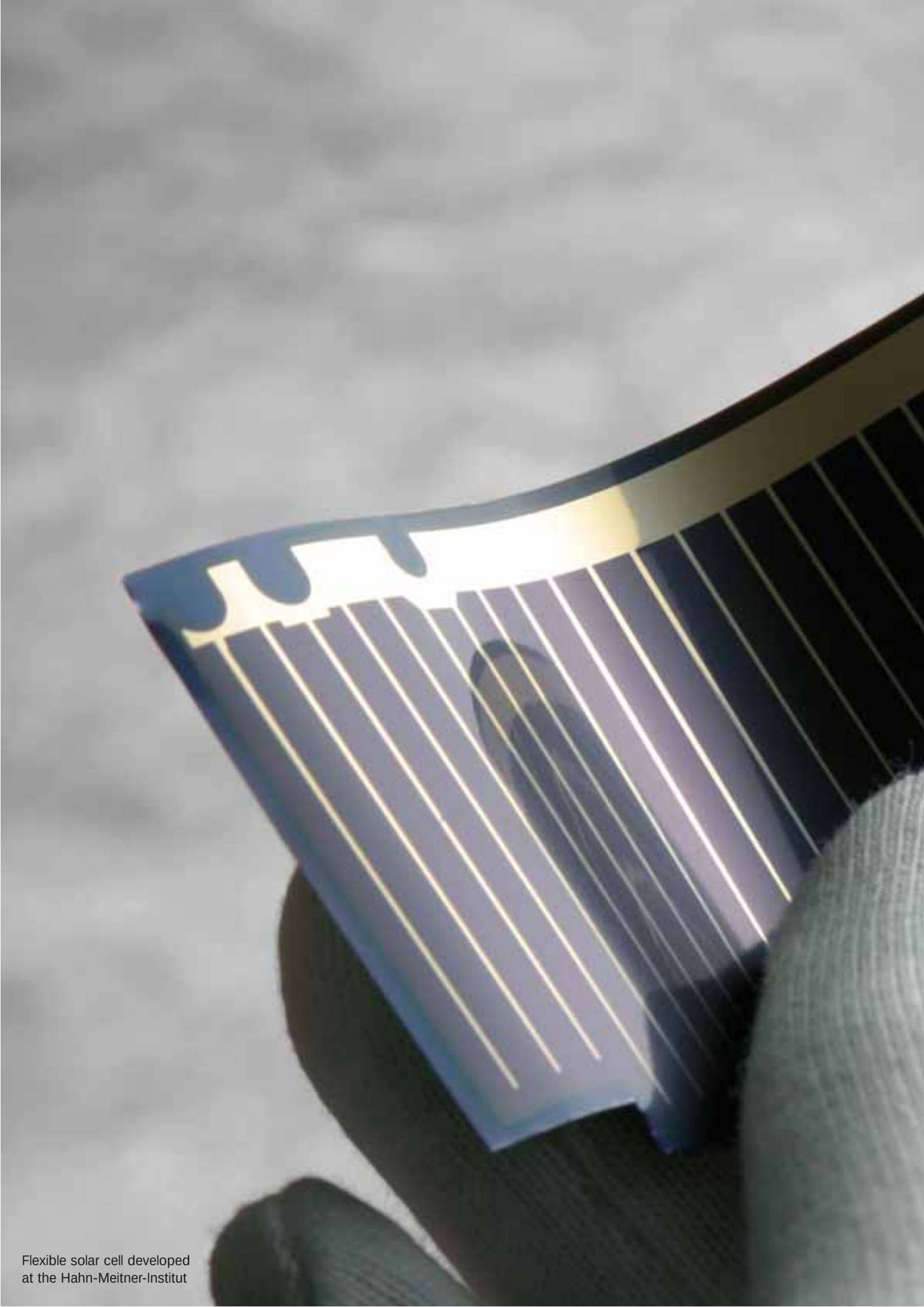

Flexible solar cell developed
at the Hahn-Meitner-Institut

Scientific highlights
Solar Energy Research 2005

Origin of preferential (100) orientation of poly-Si films made by aluminium-induced layer-exchange process

A. Sarikov[1], J. Schneider[2], J. Klein[2], M. Muske[2], S. Gall[2], W. Fuhs[2]
■ 1 On leave from V. Lashkarev Institute of Semiconductor Physics NAS Ukraine, Kiev, Ukraine ■ 2 HMI, SE1

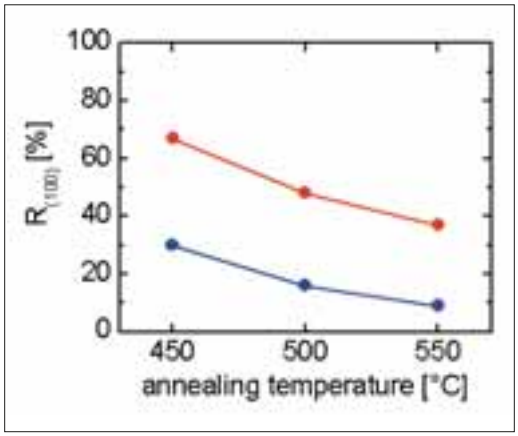

Fig. 1: Preferential (100) orientation $R_{(100)}$ as a function of the annealing temperature, T_A, for samples with native oxide (red) and thermal oxide (blue) [4]. The definition of $R_{(100)}$ is based on a 20° tilt with respect to the (100) orientation.

The formation of large-grained polycrystalline Si (poly-Si) seed layers on glass and the subsequent epitaxial thickening at low temperatures is a promising approach to create absorber layers of high electronic quality for poly-Si thin-film solar cells. The aluminium-induced layer-exchange (ALILE) process allows to form seed layers suitable for the subsequent epitaxial thickening at low temperatures (below 600°C). In the ALILE process, Al/amorphous silicon (a-Si) bi-layers on glass exchange their positions with a concurrent crystallization of the a-Si during annealing below the eutectic temperature of the Al/Si system (transformation of a glass/Al/a-Si structure into a glass/poly-Si/Al+Si structure) [1, 2]. The kinetics of this process is controlled by a thin AlO_x membrane between the initial Al and a-Si layers, obtained by oxidation of Al prior to a-Si deposition.

A characteristic feature of the poly-Si films prepared by the ALILE process is the preferential (100) grain orientation, which is very favourable for the epitaxial thickening at low temperatures [3]. The preferential (100) orientation, $R_{(100)}$, of the poly-Si layers made by the ALILE process is shown in Fig. 1, as obtained by electron back scattering diffraction (EBSD) [4] (the definition of $R_{(100)}$ is based on a 20° tilt with respect to the (100) orientation). The preferential orientation is dependent upon the annealing temperature and the way the membrane has been formed (native oxide (Fig. 1, red) and thermal oxide (Fig. 1, blue)). Lower annealing temperatures result in higher degree of $R_{(100)}$, while annealing at higher temperatures leads to more Si grains featuring other orientations.

We have proposed a simple model for the formation of the preferential (100) orientation of Si grains during the ALILE process [5], which starts from the assumption of a preferential nucleation. The nucleation of Si grains during the ALILE process occurs heterogeneously at the interface between the membrane and the grain boundaries of polycrystalline Al. We have assumed a double pyramid shape of the Si nucleus in Al, formed by {111} planes, due to the lowest surface energy of this plane [6], and considered the formation of a Si nucleus obtained by sectioning the double Si pyramid by the Al/AlO_x membrane interface. The orientation of the sectioning plane was determined by two angles, φ and θ, the rotation angle of the horizontal projection of plane normal, and the tilt angle from the vertical axes ([100] direction). The model structure is shown in Fig. 2. The formation of the critical nucleus is determined by the change of the Gibbs energy ΔG:

$$\Delta G = \sigma_{Al,Si} S_{Al,Si} + \sigma_{AlOx,Si} S_{AlOx,Si} - \gamma V$$

Here, $\sigma_{Al,Si}$ and $\sigma_{AlOx,Si}$ are the specific interface energies of Si with the Al and the AlO_x membrane, respectively, $S_{Al,Si}(\varphi, \theta)$ and $S_{AlOx,Si}(\varphi, \theta)$ are the respective interface areas, γ is the specific volume energy of Si, and $V(\varphi, \theta)$ is the nucleus volume. The first two terms describe the increase of the Gibbs energy due to the formation of the interface between Si and Al or AlO_x membrane, respectively. The third term describes the decrease of the Gibbs energy due to the Si bulk formation. The critical size of a nucleus and the corresponding critical Gibbs energy associated with nucleation, $\Delta G_{cr}(\varphi, \theta)$, at a fixed nucleus orientation relative to the Al/AlO_x membrane interface plane are determined by the maximum of the change of the Gibbs energy.

Si nuclei with minimum critical Gibbs energy are formed preferentially. Therefore, the preferential orientation of the poly-Si films is determined by the orientation of these nuclei. In Fig. 3, the dependence of the critical Gibbs energy on the tilting angle, θ, is shown for tilting in two directions, (110) ($\varphi = 0$) and (111) ($\varphi = \pi/4$). The calculations have been made using $\gamma = 3.5 \times 10^8\,J/m^3$, which corresponds to two times oversaturation of Al with Si, $\sigma_{Al,Si} = 0.2\,J/m^2$, which corresponds approximately to the interface energy of 0.1 eV/atom of the solid phase crystallisation of amorphous Si [6], and $\sigma_{AlOx,Si} = 0.5 \times \sigma_{Al,Si}$. The value of the interface energy between the Si and the AlO_x membrane was taken arbitrary, only taking into account that it should be smaller than the $\sigma_{Al,Si}$ value, to enable heterogeneous nucleation. This is justified since other values of $\sigma_{AlOx,Si}$ have an effect on only quantitative and not qualitative results.

It can be seen from Fig. 3 that the energy barrier for nucleus formation, ΔG_{cr}, is the smaller the closer is the nucleus orientation to (100). Therefore, the probability of formation of (100) oriented nuclei is larger compared to any other orientation. Especially this is true for the lower temperatures of annealing. At higher temperatures, the probability of nuclei to have orientation different from (100) increases, which can explain the experimentally observed temperature dependence of the preferential orientations of poly-Si films made by the ALILE process.

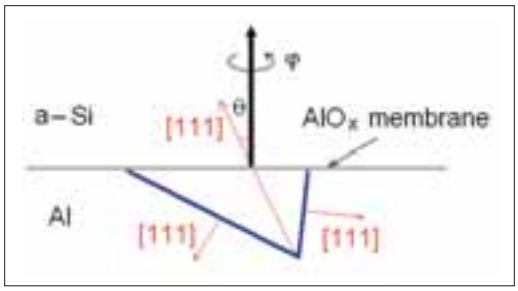

Fig. 2: Sketch of tilted pyramid. The orientation of the pyramid is determined by angles φ and θ. The picture is shown for $\varphi = 45°$.

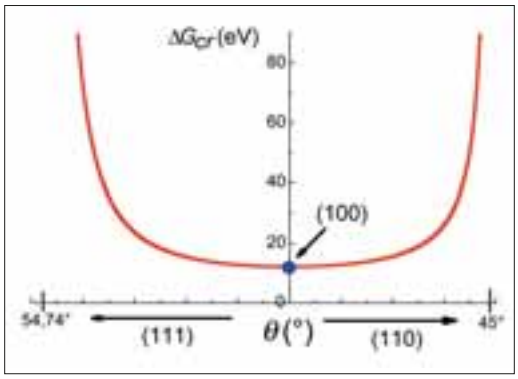

Fig. 3: Calculated critical Gibbs energy, ΔG_{cr}, as a function of the tilt angle, θ, from (100) towards (110) and (111) orientation

[1] O. Nast, S.R. Wenham, J. Appl. Phys. 88 (1), 124 (2000)
[2] J. Schneider, et al., Mater. Res. Soc. Symp. Proc. 862, A 2.2 (2005)
[3] B. Rau, et al., J. Cryst. Growth 270, 396 (2004)
[4] S. Gall et al., Thin Solid Films 511–512, 7 (2006)
[5] J. Schneider et al., J. Cryst. Growth 287, 423 (2006)
[6] C. Spinella, et al., J. Appl. Phys. 84 (10), 5383 (1998)

Corresponding author:
A. Sarikov
andrey.sarikov@hmi.de

Structural defects in crystalline silicon epitaxially grown at temperatures below 600°C

K. Petter[1], B. Rau[1], I Sieber[1], D. Eyidi[2], M. Stöger-Pollach[2], S. Gall[1], K. Lips[1], W. Fuhs[1]
■ 1 HMI, SE1 ■ 2 Technische Universität Wien, Vienna, Austria

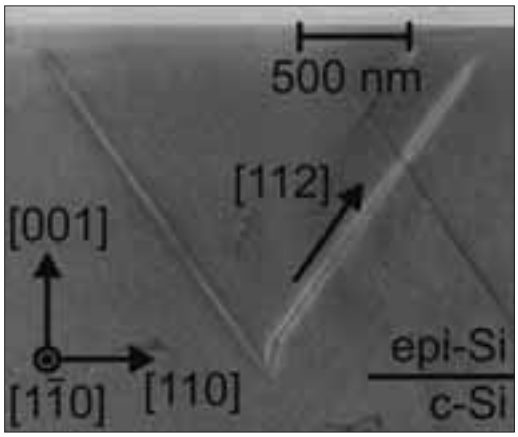

Fig. 1: TEM crossection image of an epi-Si layer on top of a c-Si wafer revealing the V-shaped defect E2 that originates at the epi-Si/c-Si interface

En route to the realisation of large-grained polycrystalline silicon thin-film solar cells on glass, deposition methods are required that enable epitaxial growth on appropriate seed layers at temperatures below the softening point of the glass substrate (~600°C). For the solar cell concept of the department such seed layers are produced from aluminium-induced crystallisation of amorphous silicon which are then epitaxially thickened by Electron-Cyclotron Resonance Chemical-Vapour Deposition (ECRCVD) [1]. This method enables low-temperature epitaxy by increasing the adatom mobility at the growth front due to low energy ion bombardment. However, a general problem is the formation of defects in the epitaxially grown silicon (epi-Si) layers. Depending on their density and electrical activity, recombination of charge carriers at such defects may severely lower the minority carrier lifetime and degrade the performance of a solar cell produced from this material. Therefore, it is most important to identify the relevant defects in epi-Si, understand their mechanism of formation and point out procedures to minimise their density.

In this work we present an investigation on line defects that develop during epitaxial growth with ECRCVD. In order to minimise influences of the non-ideal seed layer, the best possible substrate was used for epitaxy, namely a (100) oriented monocrystalline silicon (c-Si) wafer. Epi-Si layers deposited in the temperature range of 560 – 600°C are macroscopically of good crystalline quality and cannot be distinguished from perfect crystals using methods like Rutherford Backscattering or Raman investigations. However, using transmission electron microscopy (TEM) a variety of extended defects can be observed [2]. Fig. 1 exemplary shows a TEM cross section image of a V-shaped defect, called E2, that is created at the epi-Si/c-Si interface and grows in the [112] direction. Further analysis revealed that also two other types of line defects, labelled E1 and D, are present in the epi-Si layers [2]. Models of the line defects identified in epi-Si are presented in Fig. 2. Defects D and E2 are pairs of partial dislocations confining stacking faults (shaded region) with line directions of [314] and [112], respectively. Note that both start to grow at the epi-Si/c-Si interface. With secondary ion mass spectroscopy (SIMS) we revealed that there is a high oxygen concentration at the epi-Si/c-Si interface, which is probably due to a contamination of the wafer surface before deposition. Such an oxygen contamination is known to lead to the formation of dislocations in epi-Si layers [4]. In contrast to D and E2, the E1 defects have a different structure with their origin lying in the layer itself. Additional analysis using photoluminescence showed [2], that these defects are presumably so called “line interstitial defects”. These defects build up by agglomeration of self-interstitials, which are introduced into the epi-Si layers due to the low-energy ion bombardment during the growth.

In silicon solar cells, the density of extended defects in the absorber layer strongly determines device performance. A determination of defect densities in the epi-Si layers can, in principle, be accomplished by TEM. This, however, is connected with high preparative and analytical efforts. A more suitable method is defect etching, that makes use of the strained crystal region, which is always present around structural defects. Etch solutions like the so called “Secco Etch” have an anisotropic etch rate depending on the strain in the crystal. Etching the surface of the epitaxial layers therefore leads to etch pits where structural defects penetrate the surface. A scanning electron microscopy (SEM) image of the etched surface of a typical epi-Si film is shown in Fig. 3. An analysis of the form and crystallographic orientation of the etch pits makes it possible to relate the etch pits to the structural defects observed by TEM [2]. The etch pits are marked and named according to the classification shown in Fig. 2. With this identification the density of the different line defect can easily be determined.

With this procedure, we determined the dislocation density, N_D, of 2 µm thick boron-doped epi-Si layers on (100) c-Si substrate to be $4\times10^{8}\,cm^{-2}$. An as-grown solar cell prepared from these epi-Si layers had an efficiency of 4.2 % and a short circuit current of $13.0\,mA\,cm^{-2}$, which is predicted for such a high value of N_D [3]. This leads us to the conclusion that the dislocations present in the epi-Si solar cell absorber are one major factor limiting the efficiency. Simulations show, that a reduction of N_D to $10^{6}\,cm^{-2}$ should be sufficient to solve this problem [3]. In future work, we will therefore further investigate how the density of defects or their electrical activity can be reduced. Beside post deposition treatments like rapid thermal annealing and hydrogen passivation we will further optimize the wafer pre-treatments, since a reduction of the surface oxygen contamination by a factor of 10 should be sufficient to lower N_D by a factor of 100 [4].

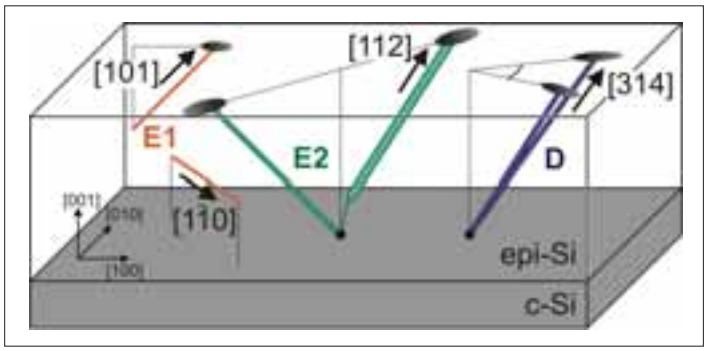

Fig. 2: Models of line defects in epi-Si layers. E1 defects are so called “line interstitial defects”, E2 and D are pairs of partial dislocations with line directions of [112] and [314], respectively.

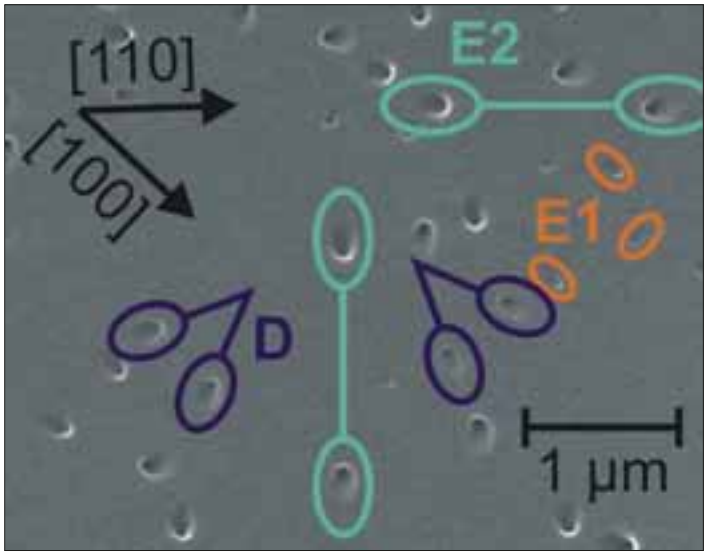

Fig. 3: Etch pits observed after treating the surface of the epi-Si layer with a defect etch. The etch pits could be assigned to the defects whose models are shown in Fig. 2.

[1] B. Rau, I. Sieber, J. Schneider, M. Muske, M. Stöger-Pollach, P Schattschneider, S. Gall, W. Fuhs, J. Crystal Growth 270, 396 (2004)
[2] K. Petter, D. Eyidi, M. Stöger-Pollach, I. Sieber, P. Schubert-Bischoff, B. Rau, A. T. Tham, P. Schattschneider, S. Gall, K. Lips, W. Fuhs, Physica B 376–377, 117 (2006)
[3] M. Imaizumi, T. Ito, M. Yamaguchi, K. Kaneko, J. Appl. Phys. 81, 7635 (1997)
[4] M. Tejwani, P. Ronsheim, Mat. Res. Soc. Symp. Proc. 259, 467 (1992)

Corresponding author:
B. Rau
bjoern.rau@hmi.de

Progress in Taking the CdS Layer out of Thin-Film Polycrystalline $CuInS_2$ Solar Cells

A. Ennaoui[1], M. Bär[1,3], J. Klaer[2], T. Kropp[1], R. Sáez-Araoz[1], H.-W. Schock[2], M.C. Lux-Steiner[1]
■ 1 HMI, SE 2 ■ 2 HMI, SE 3 ■ 3 Current address: University of Nevada, Las Vegas, USA

Introduction

At the Hahn-Meitner-Institut (HMI), the two departments SE2 and SE3 cooperate in a joint effort with the aim to eliminate the CdS window layer commonly used in $CuInS_2$ solar cell devices. This is motivated by the potential to enhance the spectral response in the blue wavelength region by the use of materials with wider band-gap than CdS ($E_g \sim 2.4\,eV$). Furthermore, CdS as a heavy metal compound should be avoided in the final solar modules as well as in their production processes. Thus chalcopyrite photovoltaic industry should not be listed in the future as a source of cadmium emission to the environment. In this work we present recent progress in Cd-free $CuInS_2$ with Zn(S,O) ($E_g \sim 3.6-3.8\,eV$) buffer layers prepared by a solution growth method known as Chemical Bath Deposition (CBD).

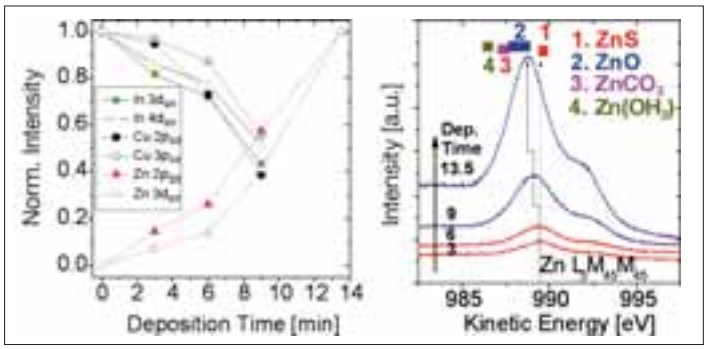

Fig. 1: left: Normalized XPS intensities signal from the attenuated substrate and attenuating Zn(S,O) top-layer. right: $Zn\,L_3M_{45}M_{45}$ Auger peak for different coverage with Zn(S,O) buffer. The regions of different Zn-compounds from the literature are indicated in bars.

CBD-Zn(S,O) growth on CIS

Background of CBD-Zn(S,O):

A typical CBD of ZnS uses ammonia (NH_3), Zn-salt ($ZnSO_4$) and thiourea (SC(NH2)2) in an aqueous solution. $SC(NH_2)_2$ is known to provide S^{2-} ions. NH_3, usually described as a cation complexing agent, plays an important role in controlling the formation of metal hydroxide and increases the rate of thiourea hydrolysis. We have originally conceived a new CBD process where $SC(NH_2)_2$ and Zn-salt form $[Zn(SC(NH_2)_2)n]^{2+}$ complexes. The new complexes act as a source of zinc and sulphur [1] and allow the formation of Zn(S,O) layer with high growth rate.

XPS analysis of Zn(S,O) on CIS:

We focused on the interface formation during the growth of the ZnS buffer onto the CIS substrate. The approach for the investigation of the CBD-ZnS/CIS interface is described in ref. [2,3]. A set of samples was characterized by X-ray Photoelectron Spectroscopy (XPS) and X-ray Auger Electron Spectroscopy (XAES) using an Mg K_α x-ray source (1253.6 eV). The buffer layer was deposited onto (KCN-etched) CIS substrates within different deposition times. The evaluation of XPS spectra in the Zn3d and In4d region reveals a complete coverage of the CIS absorber layer after 13,5 min of buffer deposition. The evaluation of the Zn $L_3M_{45}M_{45}$ XAES signal for the Zn(S,O)/CIS sample series (Fig. 1, right) shows that in the early stages of the CBD process (up to 6 min deposition time) a thin (up to 0.6 nm) ZnS layer is formed on the CIS, whereas in the second half of the CBD ("9 min" and "13.5 min" sample) Zn(S,O) is deposited with a greatly increased growth rate. This is supported by the comparison of the Zn $L_3M_{45}M_{45}$ XAES measured spectra with Zn $L_3M_{45}M_{45}$ (^1G) Auger peak of Zn-compounds possibly formed in the chemical bath (e.g., ZnO, ZnS, $Zn(OH)_2$) [4]. Fig. 1 (left) shows the normalized XPS photoemission signals of the CIS substrate and Zn(S,O) buffers. The attenuated substrate intensities ($In\,3d_{3/2}$, $In\,4d_{3/2}$, $Cu\,2p_{3/2}$, $Cu\,3p_{1/2}$) are normalized to the value of the uncovered substrate: "0 min" and the intensity of the attenuating Zn(S,O) top-layer ($Zn\,2p_{3/2}$ and $Zn\,3d_{3/2}$) XPS peaks are normalized to the value of a complete substrate coverage: "13.5 min".

The intensities of the substrate photoemission signals decrease with increasing deposition time, simultaneously the intensities of the top-layer-related Zn XPS peaks increase. Interestingly, the photoemission signals ascribed to In are more strongly attenuated by the Zn(S,O) top-layer as the ones ascribed to Cu in the initial stages of the chemical bath deposition. This finding gets even more pronounced if one takes the inelastic mean free path (IMFP) of the corresponding photoelectrons into account (according to the universal curve the IMFPs of the Cu 3p and Cu 2p photo-

electrons are smaller than those of the In 4d and In 3d photoelectrons, respectively). The thickness calculated from the attenuation of the In ($In\,3d_{3/2}$ and In 4d) photoemission lines is bigger than the one determined from the intensity behavior of the Cu ($Cu\,2p_{3/2}$ and Cu3p) XPS signals. Since a larger Zn(S,O) layer "thickness" is determined for Indium, this can be interpreted as an In migration away from the buffer/absorber interface during ZnS/Zn(S,O) deposition, a Cu migration towards the hetero-contact or even a Cu "diffusion" out of the CIS into the deposited buffer layer. The detail for this issue will be developed in Ref. [5].

Solar cell devices

All samples were prepared according to the preparation conditions described in ref. [2, 3]. Table I summarizes the device performance with Zn(S,O) buffer. The efficiencies are compared with the corresponding CBD-CdS reference cells. All the results are supported by significant statistical data. Annealing in air at approx. 200°C has positive effects on the device performance.

Buffer	Type	V_{OC} [mV]	J_{SC} [mA/cm²]	FF [%]	η [%]
Zn(S,O)	Cell	700.4	700.4	65.8	10.4
CdS		705.7	705.7	66.8	10.2
CdS	Module	671.6	671.6	66.9	9.07
Zn(S,O)		700	700	64.0	10.1

Table 1: Performance of cells and modules with CBD-Zn(O,S) buffer layer compared to CdS base line under standard conditions for AM1.5 irradiation

As expected, the CIS solar cell with alternative Zn(S,O) buffer benefits from its increased window transparency in the short-wavelength region compared to the device with CdS buffer as indicated by the higher J_{SC}. This conclusion is also supported by external quantum efficiency measurements of corresponding solar cells with Zn(S,O) and CdS buffers, respectively, which are shown in Fig. 2. The higher transparency of the Zn(S,O) buffer layer in the short-wavelength region in comparison to that of the CdS layer can clearly be seen. The difference between the respective QEs ($QE_{Zn(S,O)} - QE_{CdS}$) is also given at the bottom of Fig. 2. The area below this curve related to the solar spectrum AM 1.5 is indicative of the respective difference in J_{SC}, which is determined here to be approx. 1 mA/cm².

This improvement of J_{SC} of the devices with a Zn(S,O) buffer in comparison to the CdS buffered reference is obviously sufficient to compensate losses from V_{OC} and FF, which are still a little lower than those of solar cells with CBD-CdS buffer, resulting in a comparable efficiency. In order to determine the active area efficiency of the CIS-based device with Zn(S,O) buffer the J_{SC} (24.5 mA/cm²) extracted from corresponding QE measurements was used. In this way hactive area was calculated to 11.3 %, which is to our knowledge the (up to now) highest reported efficiency of Cd-free $CuInS_2$-based thin film solar cells with Zn-compound buffer layers.

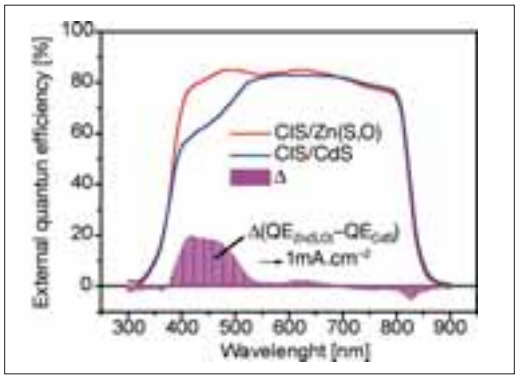

Fig. 2: External quantum efficiencies of CIS-based solar cells with Zn(S,O) and CdS buffer, respectively. The difference Δ between the two QEs is indicated.

Final remarks

The new CBD process originally conceived allowed the formation of Zn(S,O) based buffer layers on CIS absorber with high growth rate and demonstrate the potential of being as good as the conventional used CdS buffers for CIS solar cell devices. For the first time, Cd free CIS-based mini-modules yield active area (17.2 cm²) efficiency up to 10 %. The following issues are currently investigated: CBD control of oxygen to sulfur ratio, intermixing at CIS/Zn(S,O) interface and valence band offset, the impact of intermixing on the devices performances and scaling up the CBD process to large area 10×10 cm².

[1] German Patent pending: 10 2004 040 546.8-33.
[2] A. Ennaoui, M. Bär, J. Klaer, T. Kropp, R. Sáez-Araoz, and M.C. Lux-Steiner, Proc. 20th European Photovoltaic Solar Energy Conference (EPVSEC-20), Barcelona, Spain, (2005) 1882
[3] A. Ennaoui, M. Bär, J. Klaer, T. Kropp, R. Sáez-Araoz, and M.C. Lux-Steiner, Prog. Photovolt. In press
[4] M. Bär, A. Ennaoui, J. Klaer, T. Kropp, R. Sáez-Araoz, N. Allsop, I. Lauermann, H.-W. Schock, and M.C. Lux-Steiner, J. Appl. Phys., submitted.
[5] M. Bär, A. Ennaoui, J. Klaer, T. Kropp, R. Sáez-Araoz, S. Lehmann, A. Grimm, I. Lauermann, Ch. Loreck, St. Sokoll, Ch. Jung, H.-W. Schock, Ch.-H. Fischer and M.C. Lux-Stein J. Appl. Phys. In preparation

Corresponding author:
A. Ennaoui
ennaoui@hmi.de

Optimising the interface between zinc-phthalocyanine films and the transparent indium-tin oxide anode in organic solar cells

M. Vogel, B. Johnev, M. Rusu, F. Streicher, S. Sadewasser, T. Mete, Ch. Breyer, M. Ch. Lux-Steiner, K. Fostiropoulos
■ HMI, SE2

Organic solar cells are regarded as a potentially low cost technology and may play a crucial role in the photovoltaic evolution of the coming decades [1]. Scientific knowledge in this field however is much less extensive than in the case of inorganic technology. Among the most important issues for the optimisation of photovoltaic devices range the interfaces between inorganic electrodes and organic photoactive films. To ensure loss free transport of charge carriers across these interfaces, the formation of uniform, ohmic contacts without traps or defects are required.

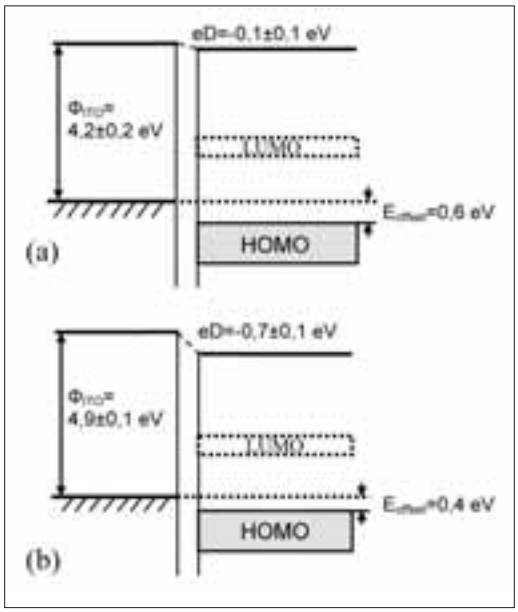

Fig. 1: Energy diagrams of ZnPc on solvent cleaned ITO (a) and of ZnPc on phosphoric acid treated ITO. ϕ: work function, eD: dipole, LUMO: lowest unoccupied molecular orbital.

In the following we focus on the interface between the transparent Indium-tin oxide (ITO) electrode and a zinc-phthalocyanine (ZnPc) film. In organic solar cells based on ZnPc and C_{60} holes need to be conducted across this interface. Judging from the work function of solvent cleaned ITO of 4.2 eV [2] and the ionization energy of ZnPc of 5.3 eV [3], a mismatch between highest occupied molecular orbital (HOMO) of ZnPc and the Fermi level in the ITO conduction band of 1.1 eV is expected. To reduce this mismatch and thus improve hole transport the work function of ITO can be increased by surface treatments, i.e. dipping ITO substrates into phosphoric acid [4]. This treatment induces the formation of a surface dipole layer and in consequence an increase of the work function by 0.6±0.1 eV [2]. Solar cell performance was thus improved by up to 40% [5].

To provide a better understanding of this effect, the interface was characterised using photoelectron spectroscopy (PES) and ultra high vacuum Kelvin probe force microscopy (UHV-KPFM). As in standard solar cell preparation [5] ITO substrates were coated with ZnPc by thermal vacuum deposition. The samples were then transferred in vacuum to the ultra high vacuum PES system and analysed by ultraviolet photoelectron spectroscopy (UPS). By fabricating a series of extremely thin (0–64 Å) ZnPc films, the UPS results yielded a detailed picture of the electronic transition from ITO to ZnPc. The resulting energy diagrams for the ITO reference sample (solvent cleaned commercial substrates) and for phosphoric acid dipped ITO are plotted in Fig. 1.

The results of the UPS measurements lead to a number of interesting conclusions. They show that the offset between HOMO of ZnPc and Fermi level of ITO is nearly the same for solvent cleaned and phosphoric acid treated ITO. It is important to note that within the accuracy of the measurement (±0,1 eV) no band bending was observed in the phthalocyanine film. However the results imply the formation of a dipole within the first monolayer of ZnPc. This dipole is about equal in magnitude and opposite in direction compared to the surface dipole of ITO induced by the acid treatment. In consequence the improvement in efficiency of solar cells produced with acid treated ITO cannot be attributed to a reduced offset at the interface. Another mechanism must be responsible for the beneficial effects of ITO acid treatment. Several hints suggest that these effects are due to the formation of a uniform interface with little defects between acid treated ITO and ZnPc: X-ray PES measurements have shown that the treatment with phosphoric acid causes a chemical reaction of acid ions with the ITO surface [2]. The resulting chemically bound monolayer proved to be very stable. UHV-KPFM measurements of phosphoric acid treated ITO yield the locally resolved work function of the sample. The resulting image is presented in Fig. 2. It confirms the work function values found by PES and in addition shows that the acid treatment leads to a very homogeneous work function with a standard deviation of only 0.019 eV.

To further optimise the ITO-ZnPc interface the approach of chemical modification of the ITO anode is continued. Currently examinations on modified, soluble ZnPc molecules with four phosphoric acid groups are in progress. The aim is to maintain the benefits of a chemically bound monolayer on ITO while at the same time establishing close contact of phthalocyanine molecules with the surface. First measurements indicate a strong increase in work function and enhanced crystallinity of ZnPc-films on thus treated ITO substrates.

[1] C. J. Brabec, Sol. Energy Mater. Sol. Cells 83, 273 (2004)

[2] M. Vogel, Dissertation Freie Universität Berlin 2005

[3] W. Gao, A. Kahn, Organic Electronics 3, 53 (2002)

[4] F. Nüesch, L. J. Rothberg, E. W. Forsythe, Q. T. Le, Y. Gao, Appl. Phys. Lett. 74, 880 (1999)

[5] B. Johnev, M. Vogel, K. Fostiropoulos, B. Mertesacker, M. Rusu, M.-C. Lux-Steiner, A. Weidinger, Thin Solid Films 488, 270 (2005)

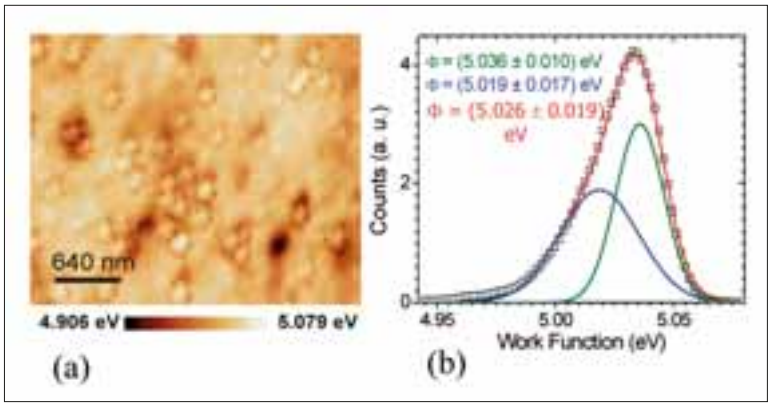

Fig. 2: (a) UHV-KPFM work function image of a phosphoric acid treated ITO surface (b) the respective histogram (b)

Corresponding author:
M. Vogel
mirko.vogel@hmi.de

On the $CuGaSe_2$-$CuGa_3Se_5$ solid state transition in CCSVT-grown $CuGa_xSe_y$ thin films

S. Lehmann[1], M. Bär[1,2], D. Fuertes Marrón[1], P. Pistor[1], S. Wiesner[1], M. Rusu[1], I. Kötschau[1], I. Lauermann[1], A. Grimm[1], S. Sokoll[1], Ch. Jung[3], Ch.-H. Fischer[1,4], Th. Schedel-Niedrig[1], M.Ch. Lux-Steiner[1,4]

■ 1 HMI, SE2 ■ 2 Department of Chemistry, University of Nevada, Las Vegas, USA ■ 3 BESSY Berlin, Germany ■ 4 Freie Universität Berlin, Germany

Cu-poor $Cu(In_{1-x}Ga_x)Se_2$ $x \approx 0.3$ films used for high performance devices reaching efficiencies of almost 20 % show a surface composition resembling to that of a 1:3:5 compound. A well established model states that a Cu-depleted surface region has beneficial effects on complete cells due to band gap widening and n-type inversion. Experimental evidence of a 1:3:5 surface composition was found in device quality $CuGaSe_2$ films [1]. However, it still remains unclear whether the presence of such a surface region has a similar positive impact on wide gap $CuGaSe_2$, as compared to its low gap counterparts. To elucidate this problem we carried out a systematic study of the impact of Cu-depletion in $CuGaSe_2$ films.

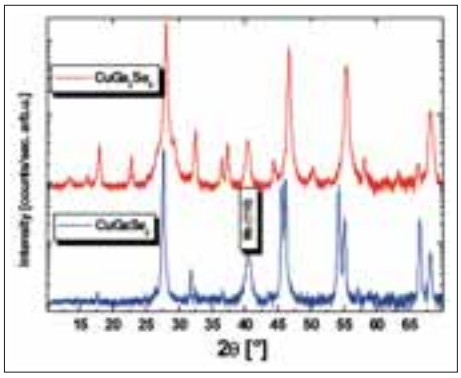

Fig. 1: XRD scans of a chalcopyrite single phase CCVST-grown $CuGaSe_2$ thin film (bottom/blue) and of an ODC single phase CCVST-grown $CuGa_3Se_5$ thin film (top/red) (measured in a Bruker D8 Advance setup with Cu-$K\alpha_{1/2}$-radiation)

Non-vacuum chemical close spaced vapour transport (CCSVT) was used for the growth of thin polycrystalline films by exposure of metallic Cu-precursors deposited on Mo-coated plain soda lime glass substrates to a $GaCl_x/H_2Se$ atmosphere [2]. The final film composition can be controlled, ranging from single phase 1:1:2 up to 1:3:5 by adjusting the process parameters. $CuGa_xSe_y$ thin films were grown in a compositional range of $1 < x < 3$. This was performed by a variation of deposition times. For analysis of the absorber backside a glass substrate was glued with silver-epoxy on the top side of selected samples. Afterwards the absorber layer was lifted-off [3] under inert N_2-atmosphere, peeling the $CuGa_xSe_y$ from the Mo back contact making the absorber backside accessible for characterization.

X-ray diffraction (XRD) spectra were recorded at a Bruker D8 Advance setup in grazing incident geometry for incident angles $\vartheta 1 = 0.5° - 2.0°$, yielding surface and bulk sensitive structural information which is strongly depth-correlated (for $\vartheta 1 = 0.5° \rightarrow$ information depth, $a = 1\,mm$ and for $\vartheta 1 = 2.0° \rightarrow a = 4\,mm$) [4, 5]. Both phases, the chalcopyrite (CCP) and the 1:3:5 ordered defect compound (ODC) can easily be distinguished from their XRD pattern (see Fig. 1), resulting from different space-group symmetries, $I\bar{4}2d$ for CCP and (proposed) $I42m$ for $CuIn_3Se_5$ [6].

An analysis of the (112) reflexion detected under grazing incident conditions of $\vartheta 1 = 0.5°$ up to 2.0° is shown in Fig. 2. By comparison of the measurements of the absorbers' front- and backside it can be clearly shown that the ODC phase is mainly located at the surface of the thin film structure (Fig. 2).

Compositional data on the [Ga]/[Cu]-ratio in the $CuGa_xSe_y$ thin films were collected by using surface sensitive X-ray emission spectroscopy (XES) (performed at CISSY / BESSY 2-U41PGM, $h\nu = 1200eV$) and bulk sensitive X-ray fluorescence (XRF) (measured with a standard Philipps MagiX-Pro X-ray fluorescence system). While the integral composition provided by the XRF measurements was based on the analysis of the K_α-fluorescence radiation of the relevant elements, the surface sensitive XES measurement used the $L_{2,3}$-fluorescence radiation of Ga and Cu. The latter detection mode has an information depth of about 900 nm [4, 5] for Ga-rich samples and for both used emission lines (Ga and Cu L_3) .

The comparison of the Cu- and Ga-L_3 emission lines from the XES spectra taken for two (in terms of integral composition) different samples at their front- and backsides reveals (see Fig. 3):
i.) The front- is Cu-poorer/Ga-richer than the backside,
ii.) The Ga-signal for the backsides of both samples is in the same range whereas for the corresponding front sides it is significantly higher.

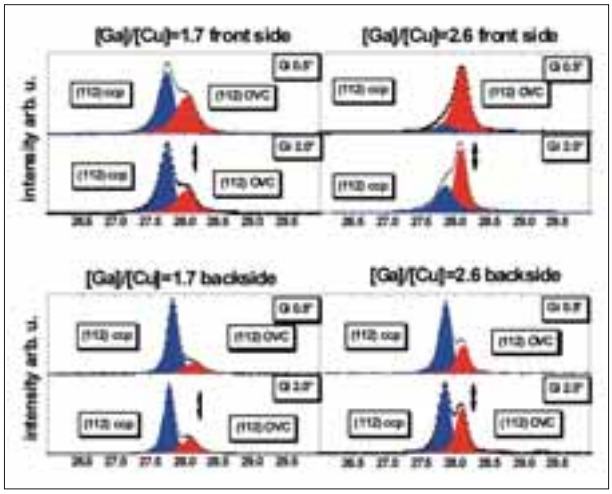

Fig. 2: Detailed XRD-scans showing the (112) reflexions of chalcopyrite (blue) as well as ODC structure (red) in grazing incident geometry for surface sensitivity [$\vartheta 1 = 0.5/0.8°$] and bulk sensitivity [$\vartheta 1 = 2.0°$]. Both were carried out for front- (top) and backsides (bottom) of CCSVT-grown $CuGa_xSe_y$ thin films with integral [Ga]/[Cu] = 1.7 (left) and [Ga]/[Cu] = 2.6 (right) (measured with a Bruker D8 Advance setup with Cu-$K\alpha_{1/2}$-radiation).

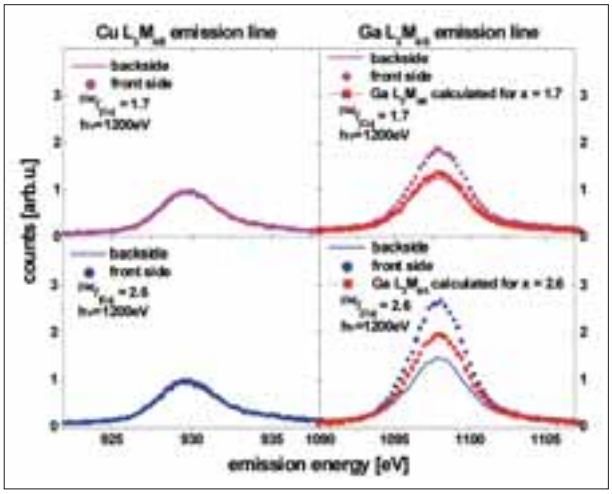

Fig. 3: XES detail spectra of Cu L_3 (left) and Ga L_3 (right) emission lines of CCSVT-grown $CuGa_xSe_y$ thin films with integral [Ga]/[Cu] = 1.7 (top) and [Ga]/[Cu] = 2.6 (bottom) (recorded at CISSY/BESSY-U41-PGM, $h\nu = 1200eV$). The spectra were normalized to the intensity of the Cu L_3 emission line.

iii.) The Ga-signal, which is simulated for the measured integral composition indicates that the sample with [Ga]/[Cu] ≈ 2.6 consists of nearly equal amounts of both phases (ODC on CCP), whereas for the sample with [Ga]/[Cu] ≈ 1.7 a thick CCP layer is covered by a relatively thin ODC layer.

Additionally, we have carried out photoelectron emission spectroscopy measurements (PES, not shown) that give information on the first few nanometres of the sample surface. This PES data always reveal a Cu-poor (surface) composition compared to that calculated from the XES data. This leads to the conclusion that the surface of all thin films, even that of a single phase ODC layer, is copper-depleted.

Based on our results, we propose a model for the $CuGa_3Se_5$ solid state phase formation for Ga-rich $CuGa_ySe_y$ CCSVT-grown thin films:
The transition from $CuGaSe_2$ to CuGa3Se5 starts with an almost stoichiometric $CuGaSe_2$ thin film where copper-depletion occurs only in the first few nanometres of the sample. Successive Ga- and Se-enrichment leads to an integral composition of the film of [Ga]/[Cu] ≈ 1.5. At this point the integral composition of the film crosses the coexistence line for the CCP single phase and the CCP/ODC two-phase region. Beyond this composition 1.5 < [Ga]/[Cu] < 3.0 an ODC phase is formed on top of the CCP film (i.e., the ODC becomes that thick that its – compared to the samples' integral – Cu-poorer composition cannot only be revealed by PES but also by XES measurements) and grows both inward and outward, as the total film thickness increases.

This process takes place until the complete layer consists of a single phase ODC, which nevertheless still shows hints for a further Cu-depletion in its near surface region.

[1] A. Meeder, L. Weinhardt, R. Stresing, D. Fuertes Marrón, R. Würz, S. M. Babu, Th. Schedel-Niedrig, M. Ch. Lux-Steiner, C. Heske, E. Umbach, J. Phys. Chem. Solids 64, 1553 (2003)
[2] M. Rusu, S. Wiesner, D. Fuertes Marrón, A. Meeder, S. Doka, W. Bohne, S. Lindner, Th. Schedel-Niedrig, CH. Giesen, M. Heuken and M. Ch. Lux-Steiner, Thin Solid Films 451–452, 556 (2004)
[3] D. Fuertes Marrón, A. Meeder, S. Sadewasser, R. Würz, C. A. Kaufmann, Th. Glatzel, Th. Schedel-Niedrig and M. Ch. Lux-Steiner, Journ. Appl. Physics 97, 094915-1 (2005)
[4] Lawrence Berkeley Laboratories internet http://www-cxro.lbl.gov/optical_constants
[5] National Institute of Standards and Technology, http://physics.nist.gov/PhysRefData/
[6] T. Hanada, A. Yamana, Y. Nakamura, O. Nittono and T. Wada, Jpn. J. Appl. Phys. 36, L1494–L1497 (1997)

Corresponding author:
S.Lehmann
sebastian.lehmann@hmi.de

Studying interdiffusion of $CuInS_2$ and $CuGaS_2$ by *in situ* diffraction

I. M. Kötschau, A. Weber, H.-W. Schock
HMI, SE3

In order to better understand the growth of chalcopyrite compounds for solar cell applications it is very useful to study the film formation in situ by energy dispersive x-ray diffraction (EDXRD). Apart from the basic understanding of $CuInS_2$ growth [1, 2] mechanism using metallic Cu/In precursors it was shown that EDXRD in conjunction with diffuse laser light scattering (LLS) helps to establish new methods for industrial process control [3]. In this report we further extend the capabilities of EDXRD to study the interdiffusion of $CuInS_2$ and $CuGaS_2$.

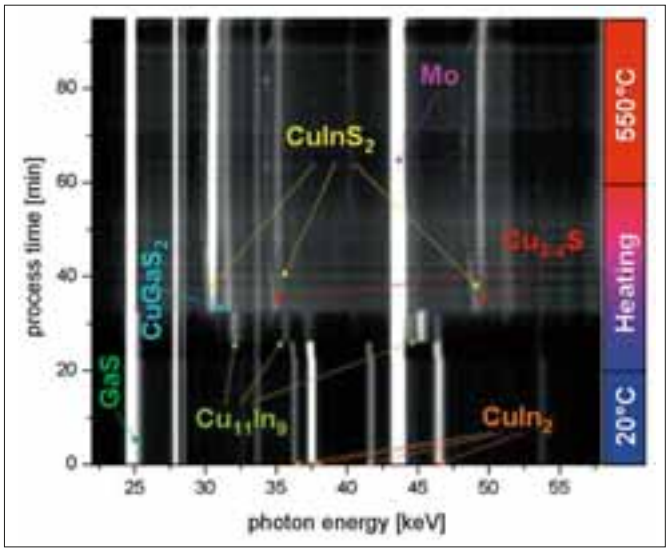

Fig. 1: EDXRD spectra as function of process time. The intensity of the peaks is provided by the grey scale. Brighter areas signify higher intensities.

The partial replacement of In by Ga in the chalcopyrite structure widens the band gap of the material [4]. Thereby the open circuit voltage of corresponding devices can be significantly enhanced [5]. In order to monitor the Ga incorporation in the a quaternary $Cu(In,Ga)S_2$ alloy we studied the phase transformations of Ga_xS_y-(Cu,In) thin film stacks annealed in sulfur vapour by *in-situ* EDXRD at the F3 beamline at Hasylab (DESY). The Ga was supplied by a crystalline (Ga_xS_y)-layer, deposited by thermal evaporation of Ga_2S_3 before sputtering elemental Cu and In precursor layers. The sulfurization was carried out in specially designed growth chamber compatible for installation at the EDXRD beamline. Typical annealing temperatures were 550°C. High resolution spectra acquired with 15 sec. integration time allow tracking of fast structural changes. Fig. 1 shows the EDXRD spectra as a function of process time. Brighter areas correspond to higher intensities. The temperature profile of the substrate is indicated by the colour code at the right axis. In the beginning of the heating phase we observe intermetallic phase transformations of the (Cu,In)-precursor. At about 260°C the diffraction signals of the $Cu_{11}In_9$ phase disappear. At the same time we observe the almost simultaneous formation of a secondary $Cu_{2-x}S$ phase and a $CuInS_2$ phase stacked on top of a $CuGaS_2$ phase. A very interesting finding is, that time evolution of the phases is significantly different when amorphous Ga_xS_y precursors are used. For longer annealing times (of crystalline Ga_xS_y) the EDXRD-spectra show the appearance of a third, intermediate $Cu(In,Ga)S_2$ phase and the diffusion of Ga into the $CuInS_2$. The diffusion process can be monitored by comparison of the lattice parameters as function of time during the annealing phase. Therefore the (110) diffraction signal of the sputtered Mo substrate with its known thermal expansion coefficient allows a precise conversion of all other energy positions into the corresponding lattice parameters. For better comparison the lattice parameters where converted to 2θ Bragg angles for chalcopyrite phases, the temperature profiles of the substrate and the LLS transient as a function of process time. The intensity of the diffraction signal is colour coded. Low intensity corresponds to dark blue and high intensities to saturated red as indicated by the colour scale. During the heating phase the thermal expansion leads to decreasing scattering angles for all three phases. Upon cooling the effect is reversed. However during the annealing phase the temperature is fixed, so that changes in the lattice constant (scattering angle) can be interpreted in terms of interdiffusion processes. The model for the fitting algorithm required to fix the lattice parameter of the intermediate, more Ga-rich, $Cu(In,Ga)S_2$ phase in the center of the stronger signals of the $CuGaS_2$ and $CuInS_2$ phases. During the annealing phase we observe a mode-

rate increase of the $CuInS_2$ scattering angle while the position of the $CuGaS_2$ signal remains nearly constant. This can be interpreted in terms of an interdiffusion process since Ga incorporation reduces the lattice parameter of pure $CuInS_2$. As Ga diffuses upwards to the top of the film, the topmost part of the $CuGaS_2$ layer is converted to a quaternary $Cu(In,Ga)S_2$ layer with high Ga content and the $CuInS_2$ on top is transformed into a $Cu(In,Ga)S_2$ alloy with low Ga content. The shift of the $CuInS_2$ peak is still small. However, the overall amount of Ga was limited to yield a homogeneous Ga/(Ga+In) ratio of 0.15. Fig. 3 depicts schematically a preliminary summary of the phase transformations the Ga_xS_y-(Cu,In) precursor annealed in S atmosphere using crystalline Ga_xS_y layers. The findings serve as input for the preparation of quaternary $Cu(In,Ga)S_2$ alloys by reactive annealing.

[1] HMI Annual Report 2003
[2] E. Rudigier, J. Djordjevic J., C. von Klopmann, B. Barcones, A. Pérez-Rodríguez and R. Scheer, Journal of Physics and Chemistry of Solids 66, 1954–1960 (2005)
[2] HMI Annual Report 2001
[3] M. Turcu, I.M. Kötschau and U. Rau, J. Appl. Phys. 91, 1391–1399 (2002)
[4] A. Neisser, PhD Thesis, Freie Universität Berlin (2002)

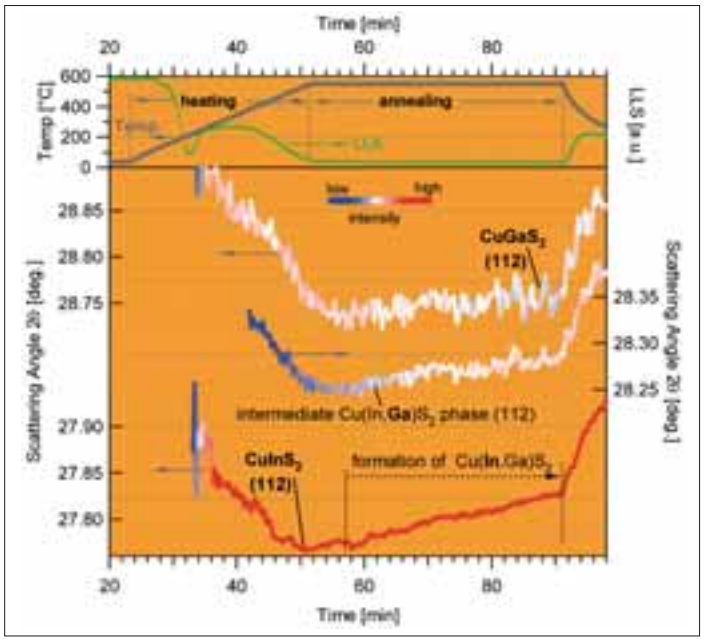

Fig. 2: Calculated peak positions for Cu-Kα wavelength, substrate temperature and LLS transient as a function of process time. $CuGaS_2$ has a higher scattering angle and thus a smaller lattice parameter as $CuInS_2$. The increasing scattering angle of the $CuInS_2$ signal during the annealing phase indicates therefore an interdiffusion process of Ga into $CuInS_2$ to form a quaternary $Cu(In,Ga)S_2$ alloy. The relative intensity of the phases is provided by the colour code.

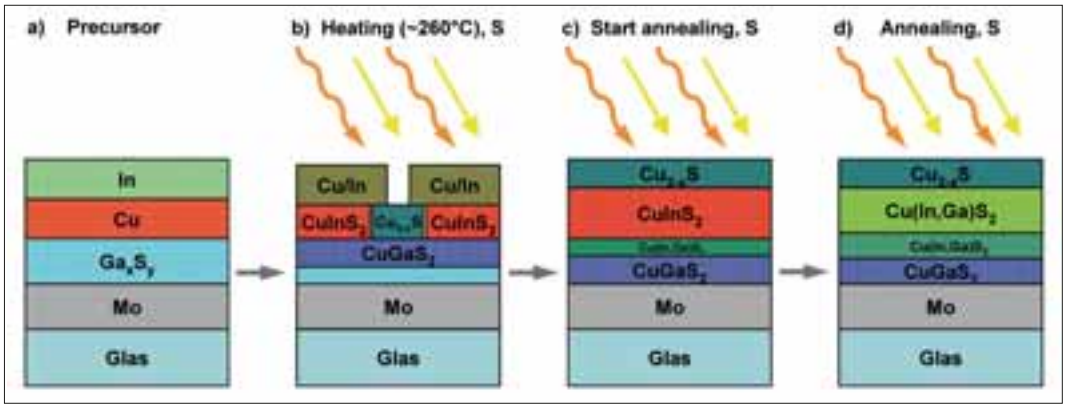

Fig. 3: Schematic representation of the phase transformation during Annealing of Ga_xS_y-(Cu/In) precursor layers in S vapour. a) Precursor as deposited. b) During the heating phase after the first $CuGaS_2$, $CuInS_2$ formation. The secondary and quasi-liquid $Cu_{2-x}S$ phase supports a fast chalcogen- and metal transport. c) During the annealing phase the part of the $CuGaS_2$ phase is transformed into an intermediate Ga-rich $Cu(In,Ga)S_2$ alloy. d) For longer annealing times the Ga diffuses into the $CuInS_2$ and forms a Ga-poor quaternary $Cu(In,Ga)S_2$ alloy.

Corresponding author:
I. Kötschau
koetschau@hmi.de

A flexible, $Cu(In,Ga)Se_2$ based, thin film solar cell module

C. A. Kaufmann[1], A. Neisser[1], K. Sakurai[1], P. Körber[1], H.-W. Schock[1], R. Klenk[2], M. C. Lux-Steiner[2]
■ 1 HMI, SE3 ■ 2 HMI, SE2

In the past few years space industry has shown increased interest in flexible $Cu(In,Ga)Se_2$ (CIGSe) thin film solar cells due to the specific advantages that devices of this type offer. Space applications require a technology that, above all, has a high specific power, i.e. it needs to be light and at the same time has to show a high efficiency. Further more it needs to be tolerant to space radiation in order to ensure minimum degradation while on orbit. Flexible thin film solar cells seem to have the potential to fulfill all these criteria. Still, they are not only of interest for space applications but wherever mobile generation of electrical power is required and weight is an issue. An efficient, robust, cheap, light, flexible and thus unbreakable, solar generator would immensely broaden the range of applicability of solar power generators across all types of applications. Therefore the HMI is currently working on the development of high efficiency $Cu(In,Ga)Se_2$ thin film modules on Ti-foil substrates. Our aim is to demonstrate that high efficiency flexible modules present an attractive technology for wide terrestrial use.

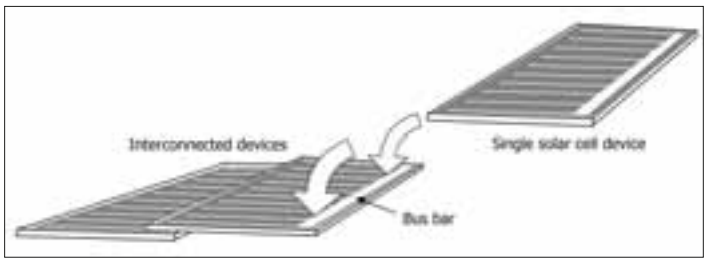

Fig. 1: Schematic for illustration of shingle-like interconnection of single cells for module integration

A primary reason for the choice of titanium as substrate material for CIGSe thin film solar cells is that the thermal expansion coefficient of titanium matches that of CIGSe [1]. Hence stress within the multi-layered device structure is kept low, even in extreme thermal environments and in particular also during fabrication. The conductivity of the substrate enables a roof-tile-like interconnection of large area, single devices as a method for module fabrication. A schematic for shingle-like interconnection of single cells for module integration is shown in Fig. 1. The bus bar of the lower device is connected to the back of the top device using a simple soldering process with indium as the filler metal. Shingle-like interconnection is an alternative to monolithic integration, an elegant interconnection technique that uses the inherent advantage of the multi-layered structure of the thin film device but which, on conductive substrates, would require an additional insulation layer between device and substrate. Insulating flexible substrates, as for example polyimide foil, on the one hand ideal for monolithic integration, are on the other hand not stable at the process temperatures that are necessary in order to produce a high quality absorber.

Fabrication processes for established high efficiency thin film devices are not easily transferred from the rigid glass substrate to the flexible titanium foil. Nevertheless, for small area devices, the transfer is achieved without efficiency loss [2,3]. In addition to that, activities to manufacture high quality flexible devices with a larger area have been successful [3,4]. The single, flexible CIGSe thin film solar cell devices presented here are prepared on a $25\,\mu m$ thick titanium foil, and consist of a stacked layer sequence in the order Mo/CIGSe/CdS/i-ZnO/ZnO:Ga. The transparent front and the back contact are both sputtered, the CdS buffer layer is deposited by chemical bath deposition and the CIGSe absorber layer is deposited using a 3 step co-evaporation process. Prior to the absorber layer deposition a sodium containing precursor is evaporated onto the Mo back contact. In addition to that a Ni/Al grid is evaporated onto the finished devices in order to facilitate current collection. Laser light scattering (LLS) is used as an in-situ process control during the PVD process [5].

Due to the fact that after shingle-like interconnection the bus bar is completely shaded by the active part of the top device, its area is not taken into account for the determination of the total area of the single cell device of $27.1\,cm^2$. A string of 4 cells with a total module area of $130\,cm^2$ thus has an aperture area of $108.4\,cm^2$. Fig. 2 shows a fully assembled module after encapsulation.

Fig. 2: Encapsulated, flexible CIGSe thin film solar cell module; total area 130 cm^2 and aperture area 108.4 cm^2

When scaling up the device from a small lab size, loss mechanisms such as the series resistance of the front grid, lateral inhomogeneities of device parameters due to material non-uniformities and last but not least an increased probabilty for localized leakage currents due to defects incorporated into the device come into play [6]. So far, a maximum efficiency of 15.0 % (AM 1.5) has been measured at the HMI for a flexible CIGSe thin film device with 27.1 cm^2 total area [3]. Using roof-tile-like interconnection, a module was fabricated with 4 single cell connected in series and showed an efficiency of 10.5 % (130 cm^2), measured before encapsulation. This correlates with a specific power of ~500 W/kg (without encapsulation) and an aperture area efficiency of 12.6 %. Fig. 3 shows the corresponding *I-V*-characteristic and related parameters. In conclusion we have shown that the flexible $Cu(In,Ga)Se_2$ thin film solar cell technology represents a viable future option to enhance power supply technologies for mobile outdoor applications.

In order to achieve the technology transfer from the rigid glass to the flexible titanium foil substrate, several issues had to be resolved [3]. For example, localized leakage currents were initially observed to limit the flexible device's performance by reducing the parallel resistance R_p. R_p is generally determined via *I-V*-measurements in the dark. These leakage currents were found to originate from defects of the surface of the titanium foil substrate. Having introduced a conditioning step for the foil surface onto which the solar cell is to be deposited, parallel resistances of > 1 kΩcm² could be reached on large area devices. Nevertheless a parallel resistance as low as 100 Ωcm² has in many cases been proven to be sufficient in order to reach efficiencies > 10 % under standard AM 1.5 conditions.

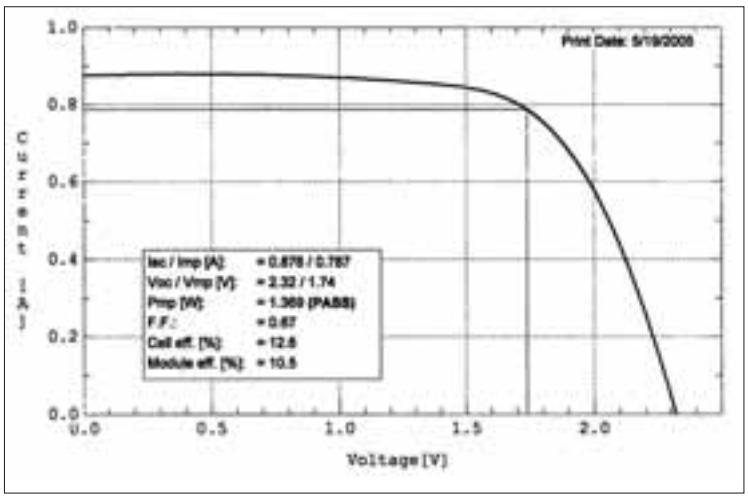

Fig. 2: *I-V*-characteristic of 130 cm^2 flexible CIGSe module

[1] M. Hartmann, M. Schmidt, A. Jasenek et. al.; Proc. 28th IEEE PVSC 638, Anchorage (2000)
[2 C. A. Kaufmann, A. Neisser, R. Klenk, R. Scheer; Thin Solid Films 480–481, 515 (2005)
[3] A. Neisser, C. A. Kaufmann, R. Klenk et al.; Proc. 7th EPSC, Stresa (2005)
[4] C. A. Kaufmann, A. Neisser, R. Klenk et al.; Proc. MRS Spring Meeting, San Francisco (2005)
[5] K. Sakurai, R. Hunger, R. Scheer et al.; Prog. in Photovoltaic: Res. & Appl. 12, 219 (2004)
[6] A. Neisser, C. A. Kaufmann, R. Klenk et al.; Proc. 31st IEEE PVSC, Florida (2005)

Corresponding author:
C. A. Kaufmann
kaufmann@hmi.de

Low band gap InP-based multi-junction solar cells

U. Seidel, H. J. Schimper, U. Bloeck, K. Schwarzburg, T. Hannappel
HMI, SE4

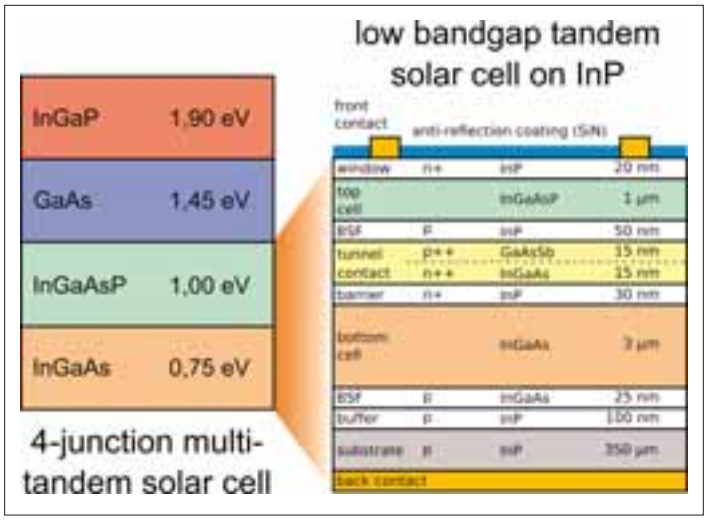

Fig. 1: The solar spectrum could be exploited more efficiently than in the current GaAs-based world record triple solar cell when combining a GaAs-based top cell with higher band gaps and an InP-based tandem bottom cell with lower band gaps

Three junction devices grown lattice-matched to GaAs on an Ge-based bottom cell have recently shown world record conversion efficiencies of around 39 % under concentrated sunlight [1]. Even higher efficiencies are expected when employing more than 3 junctions. However, cell concepts with more than 3 junctions are in demand for an absorber material with a band gap around 1 eV. Extensive studies have been conducted to use N-containing III-V material lattice-matched to GaAs. Unfortunately, the diffusion lengths in these delicate dilute semiconductor compounds remain far too low. In an alternative approach compounds with different lattice constants can be combined either by mechanical stacking, grading techniques, wafer bonding [2] or via separation of the optical spectrum [3]. However, much less efforts have been made to develop low band gap, InP-based multi-junction solar cells (MJSC) so far. Our idea aims at an interconnection of two MJSC on different lattice constants, i.e. a well-established, GaAs-based high band MJSC ($E_{gap} > 1.4$ eV) and a low band gap MJSC prepared on the lattice constant of InP. Fig. 1 shows our idea of a 4-junction MJSC design: The bottom cell is a tandem consisting of InGaAs and InGaAsP pn-junctions grown lattice-matched to InP. The upper tandem consists of GaAs and InGaP subcells. Here, we report on preliminary results obtained with a newly designed low band gap tandem structure. Once optimized, the complete cell shown in Fig. 1 is expected to give well above 40 % efficiency under concentrated sunlight. Extending the concept to 5 or 6 junctions, surpassing the 50 % efficiency limit seems possible.

III-V materials were grown by MOCVD in an Aixtron AIX-200 reactor using non-gaseous precursors that are much less toxic and more economical than conventional gaseous precursors. Fig. 2 shows the internal quantum yield of an InP cell grown with tertiarybutyl-phosphine (TBP) and trimethyl-indium (TMIn) (red curve) in comparison to the best InP cell reported in the literature (blue curve) [4]. While earlier attempts with non-gaseous precursors were less successful (green curve) [5], our result demonstrates that very good results can indeed be obtained with these advantageous precursors. Fig. 3 shows the quantum efficiency of single pn-junction cells made of the absorber materials employed in our low band gap tandem. The red curve in Fig. 1 shows the signal for the material with the lowest

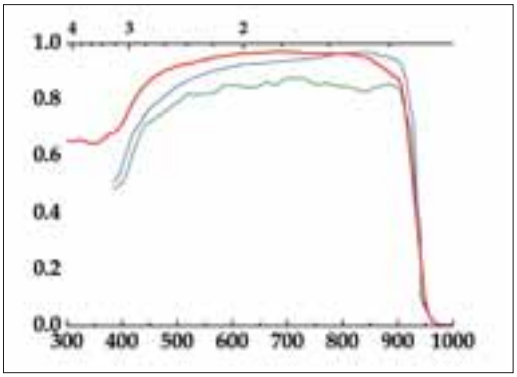

Fig. 2: Internal quantum efficiency (IQE) of an InP n/p solar cell (red) [5] compared to the IQE of the best InP cell reported in the literature (blue) [3] and the formerly best InP cell prepared with TBP (green) [4]

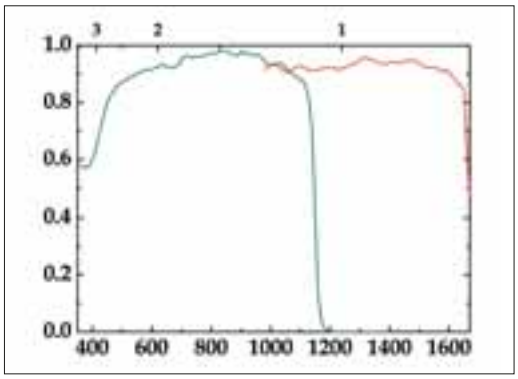

Fig. 3: Internal quantum efficiency (IQE) of an InGaAs cell (red) with an absorber layer thickness of 2 µm and IQE of an InGaAsP cell (green)

band gap, InGaAs ($E_g = 0.75$ eV), grown on p-InP(100). The green curve in Fig. 3 shows the result for the quaternary '1 eV material', i. e. $In_xGa_{1-x}As_yP_{1-y}$ (E_{gap}=1.08 eV, $x = 0.83$, $y = 0.37$). Different single junction cells with virtually the same band gaps were prepared with GaAsSb ($E_{gap} = 0.75$ eV) and InAlGaAs ($E_{gap} = 1.1$ eV) [6]. Although the performance of these less explored materials was promising [6], more optimization is needed before they would be employed equivalently in our multi-junction structure.

The low band gap tandem solar cell of Fig. 1 was grown monolithically on a p-InP(100) substrate. In this structure the subcells are connected via a hetero tunneling structure consisting of thin layers of p-GaAsSb and n-InGaAs. This asymmetric material combination was used because of the favorable band offsets. The GaAsSb layer of the tunnel junction was grown at T = 500°C to achieve best layer quality. All other layers of the solar cell were grown at a temperature of T = 600°C. After processing a SiN antireflective coating was deposited on top. The influence of different preparation procedures on the critical GaAsSb-InP hetero-interface and on the cell performance was investigated in detail, in particular by reflectance difference/anisotropy spectroscopy (RDS/RAS). First results with this low band gap tandem solar cell are represented in Fig. 4. It shows the I-V characteristic under full AM1.5g spectrum (blue) and in addition the response to filtered AM1.5g illumination. For the latter measurement a RG850 (Schott) filter was used to simulate the operation below a GaAs top cell. An open circuit voltage of 694 mV, a short circuit current density of 15.2 mA/cm², a fill factor of 76 %, and a solar conversion efficiency exceeding 8 % was in-house measured underneath the GaAs-adequate filter. Measurements were carried out with the in-house solar simulator (SE2). This is already a significant improvement of the performance of a Ge-based bottom cell ($\eta < 5$ %) that is employed in the Ge-based world record triple cell [7]. Further improvement of our low band gap tandem seems possible and under concentrated sunlight the efficiency would be even higher either way. Thus, the potential to enhance the conversion efficiency of a complete 4-junction cell as illustrated in Fig. 1 well above 40 % appears obvious. *The band gap of InGaAsP can be tuned in a wide range between 0.75 eV and 1.4 eV while maintaining the lattice match to InP [6]. This gives the opportunity to further improve the efficiency by using a 3 junction low bandgap cell.*

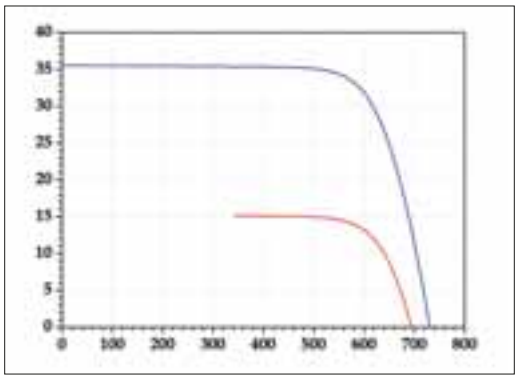

Fig. 4: I-V characteristic of an InGaAs/InGaAsP tandem solar cell measured under a full (blue curve) and a filtered (red curve, RG850) AM 1.5 g spectrum

[1] R. R. King et. al., Conference Proceedings, 20th European Photovoltaic Solar Energy Conference, Barcelona, 118–123 (2005)
[2] J. M. Zahler, A. Fontcuberta i Morral, Chang-Geun Ahn, H. A. Atwater, M. W. Wanlass et al., Ncpv and solar program review meeting proceedings, 723 (2003)
[3] L. Fraas, J. Avery, H. Huang, E. Shifman, K. Edmondson et al., 20th european photovoltaic solar energy conference and exhibition, 476 (2005)
[4] C. J. Keavney, V. E. Haven, S. M. Vernon, Proc. 21st IEEE PV Specialists Conf. IEEE, Kissimmee, FL, USA, 141 (1990)
[5] R. W. Hoffman, N. S. Fatemi, D. M. Wilt, P. P. Jenkins, D. Brinker, D. A. Scheiman, Proc. 24th IEEE PV Specialists Conf., IEEE, Waikoloa, HI, USA, 1882 (1994)
[6] H.-J. Schimper, Z. Kollonitsch, K. Möller, U. Seidel, U. Bloeck, K. Schwarzburg, F. Willig, T. Hannappel, J. Cryst. Growth (2005) online available, DOI: 10.1016/j.jcrysgro.2005.10.121
[7] C. Baur, M. Meusel, F. Dimroth, A. W. Bett, Conference Record of the 31st IEEE PV Specialists Conf., IEEE, Piscataway, NJ, USA, 675 (2005)

Corresponding author:
T. Hannappel
hannappel@hmi.de

Binding geometry of phosphonic and carboxylic acid groups on rutile TiO_2

L. Gundlach, R. Ernstorfer, R. Eichberger, S. Felber, F. Willig
■ 1 HMI, SE4

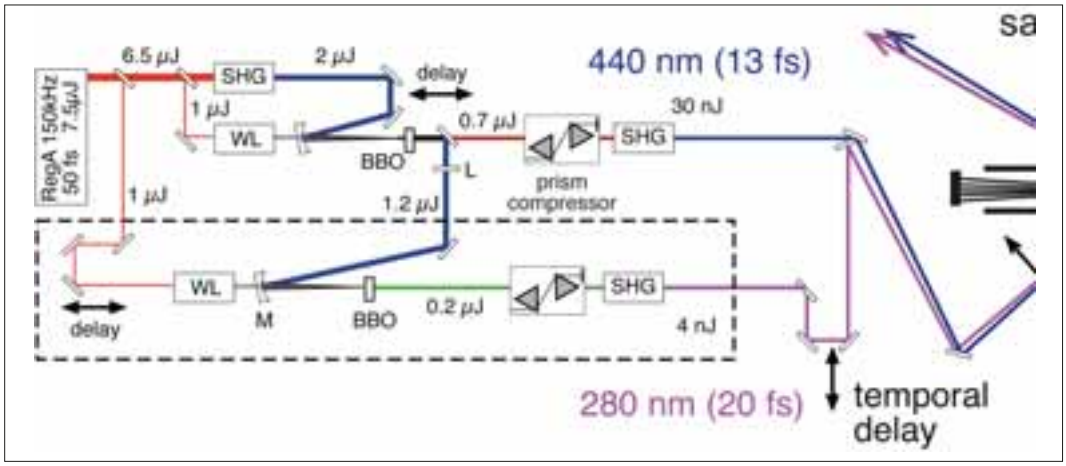

Fig. 1: Experimental setup consisting of two 150 kHz NOPAs both pumped with a 400 nm SHG pulse illustrated (left hand side) and a UHV chamber equipped with a time of flight spectrometer (right hand side)

The exact knowledge of the binding geometry of adsorbates bound chemically to metal or semiconductor surfaces is of crucial importance for understanding most relevant processes like electron transfer and photocatalytic reactions. Heterogeneous electron transfer is the first step of the charge separation in dye-sensitized solar cells (DSSC) like the Grätzel cell [1]. A detailed investigation of the binding geometry of adsorbed molecules requires a well ordered sample, unless single molecules are investigated.

Here we report on a model system for DSSC, i.e. rutile single crystal TiO_2 sensitized with a specially tailored perylene dye. This model system was selected because of its favourable spectroscopic properties and extensively investigated in our group mainly with transient absorption spectroscopy and time-resolved two-photon photoemission spectroscopy (TR-2PPE) for investigating the charge transfer and transport processes at these interfaces. For measuring the adsorption geometry angular resolved 2PPE was used. 2PPE is a pump-probe technique where a first ultrashort laser pulse excites an electron to a normally unoccupied state and a second ultrashort probe pulse lifts the electron above the vacuum energy of the sample. The emitted electron is detected in a time of flight detector (TOF).

To get angular resolution the sample was rotated in front of the electron analyzer. The position on the sample where the electron spectra were taken consequently changed slightly with changing the angle. Therefore, spectra with s- and p-polarized pump pulse were recorded and subtracted assuming that background emission is not polarisation dependent. A prerequisite to determine the adsorption geometry with this method is the knowledge of the direction of the transition dipole moment for the molecular excitation step. For perylene this is along the long molecular axis. Consequently, molecules that stand upright on the surface, e.g. perylene-carboxylic acid, can not be excited with s-polarized pump pulses and yielded no 2PPE signal originating from the molecule. The resulting 2PPE yield W versus rotation angle θ is proportional to the electric field of the pump pulse at the surface E_z^{pump} projected onto the transition dipole moment μ_z^{ion} (for details see [2]):

$$W \propto |E_z^{pump} \mu_z^{ex}|^2 \times W^{ion} \qquad \text{Eq.1}$$

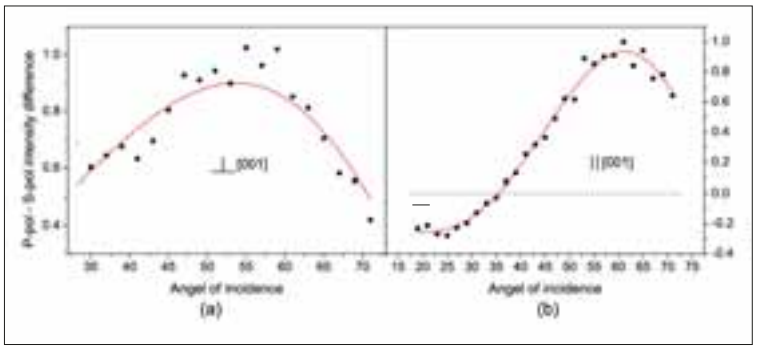

Fig. 2: Peak height of the 2PPE difference signal between p- and s-polarized pump pulse as a function of the angle of incidence for Pe'-rod on rutile (black), measured with the plane of incidence perpendicular (a) and parallel (b) to [001]. Red Curve: Calculated response (Eq. 2).

Upright bonding geometry could be verified for three different dyes with different spacer groups attached to the (110) surface of rutile via carboxylic acid groups. Latter result is in very good agreement with the reported bridging geometry of formate on the (110) surface of rutile resulting in a $p(2x1)$ LEED pattern [3].

The same measurements were performed on a perylene derivative (4-{4-[4-(8,11-Di-tert-butylperylen-3-yl)-phenyl]-bicyclo[2.2.2]oct-1-yl}-benzyl)-phosphonic acid) equipped with an other anchor group extensively investigated in our group, i.e. phosponic acid (Fig. 2). Phosphonic acid can bind via three oxygen atoms in a triangular conformation, but considering the surface structure of TiO_2 (110) the five-coordinated Ti_{4+} atoms are arranged in rows. Nilsing et al. performed DFT calculations to study the binding geometry of phosphonic acid on anatase (101) surfaces [4]. They have reported that a monodentate geometry with two hydrogen bonds and one metal: oxygen bond is the strongest configuration. Accordingly, one would expect a tilted configuration with the tilt angle perpendicular to the the [001] axis (c.f. Fig. 3). In this case the expected 2PPE yield reads:

$$W \propto \left(|E_z^{pump}\mu_x^{ex} + E_z^{pump}\mu_x^{ex}|^2 - |E_y^{pump}\mu_y^{ex}|^2\right) \times |E_z^{pump}\mu_x^{ex} + E_z^{pump}\mu_x^{ex}|^2 \qquad \text{Eq.2}$$

It should be mentioned that, because of the lack of knowledge concerning the exact direction of the transition dipole moment for the ionization step with respect to the main axis of the molecule and the alignment of the molecular plane with respect to the surface, the rotation angle of the ionization dipole moment is not well defined. However, for the sample with the plane of incidence parallel to [001] (see Fig. 2 (b)) the tilt angle of the long molecular axis with respect to the surface normal can be measured quite reliable because the pole of Eq. 2 depends only on the excitation step.

In summary, from the angular-resolved measurement the bonding geometry of the perylene dye bound via a phosphonic acid group to the TiO_2 rutile (110) surface could be deduced. The long molecular axis is tilted against [110] with an angle of around $58°$ in the direction perpendicular to the oxygen rows. This configuration is compatible with a bi- as well as a monodentate binding geometry with one or two hydrogen bonds, respectively. A balls and sticks model for the perylene dye bound with a bidentate configuration onto the TiO_2 surface is shown in Fig. 3.

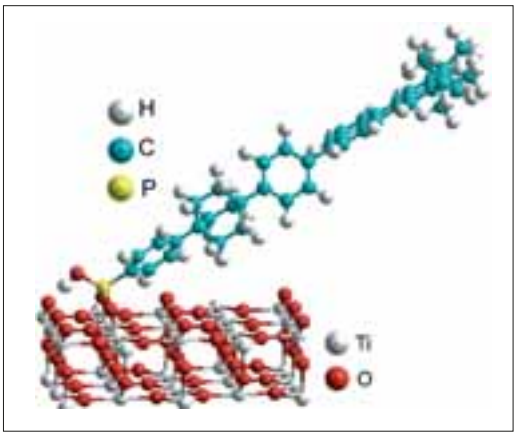

Fig. 3: Geometry of bidentate adsorbed DTB-Pe-rod on rutile (110) TiO_2 deduced from our 2PPE measurements

[1] B. O. Regan and M. Grätzel, Nature 353, 737 (1991)
[2] L. Gundlach, PhD thesis, Freie Universität Berlin (2005)
[3] H. Onishi, T. Aruga, C. Egawa, Y. Iwasawa, Surf. Sci. 193, 33–46 (1988)
[4] M. Nilsing, S. Lunell, P. Persson, L. OjamÄae, Surf. Sci. 582, 49 (2005)

Corresponding author:
F. Willig
willig@hmi.de

Ultrafast electron transfer via a bridge-extended donor orbital

R. Ernstorfer, L. Gundlach, R. Eichberger, S. Felber, F. Willig
HMI, SE4

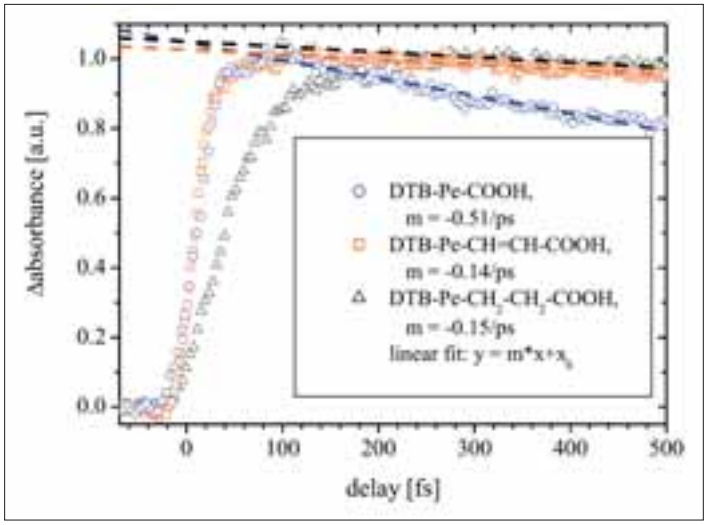

Fig. 1: Rise and early decay of the absorption of the product state of heterogeneous electron transfer, i.e. the cation of perylene, for DTB-perylene attached to TiO_2 via different bridge-anchor units. The fit to the pump-probe signals showed an injection time of 10 fs for -CH=CH-COOH, of 57 fs for -CH-CH-COOH, and of 13 fs for -COOH. Recombination rate as shown in the figure.

Transport of electrons through molecular bridges (wires) of different chemical nature is an important topic for the postulated field of molecular electronics [1] and may be of high relevance for improving dye sensitized/organic solar cells. We report here on transient absorption experiments probing electron transfer via different molecular bridges in UHV. Electron transfer occurred from the excited singlet state of the aromatic chromophore perylene to nano-sized particles of anatase TiO_2. The chromophore was linked covalently to a carboxylic group, which binds to surface Ti atoms and thus functions as the anchor group. Optionally, bridge groups were inserted in-between the perylene backbone and the anchor group. Three different experimental systems were compared: firstly, no bridge, secondly a conjugated -CH=CH- bridge unit, and thirdly a saturated -CH_2-CH_2- unit. Bulky side groups were attached to the perylene chromophore (2,5-bitertiary-butyl-perylene-9-yl, DTB-Pe) to prevent the formation of dimers by neighboring perylene chromphores on the surface. A particularly attractive feature of the perylene/TiO_2 system is the validity of the so called “wide band limit”, which is realized if the molecular donor level is energetically far above the conduction band minimum compared to the width of the electron transfer spectrum [2]. In this regime the electron transfer time is controlled by the strength of the electronic coupling and not by the magnitude of individual Franck-Condon factors [2]. UPS measurements revealed that for all three investigated systems the donor level is at least 700 meV above the conduction band minimum. The electron transfer time was determined from the time-resolved rise of the absorption signal of the ionized perylene at around 570 nm, i.e. the molecular product state of electron transfer. Our group has shown before that the absorption spectra for the ground state, the excited singlet state, and the cationic state of the chromophore perylene are spectrally well separated from each other. The laser pump (central wavelength 435 nm) and probe (central wavelength typically at 570 nm) pulses were generated with two NOPAs at a repetition rate of 150 kHz and the crosscorrelation (FWHM) was typically in the range of 25 to 30 fs.

Fig. 1 shows the time-dependent absorption of the perylene cation for the three investigated systems. There are characteristic differences in the rise (electron injection) and decay (recombination) for the two different bridge units. Electron injection via the carboxyl anchor group alone gave a time constant of 13 fs, whereas 10 fs were determined when the -CH=CH- bridge unit was inserted. In contrast, electron transfer in the presence of the $-CH_2-CH_2-$ bridge unit was found to be much slower with a time constant of 57 fs. The spatial separation of the perylene ring structure from the TiO_2 surface was most likely comparable for the conjugated and the saturated bridge units and the recombination rate observed in this early time window is almost identical for both bridges. The extension of the donor orbital onto the conjugated bridge can be seen in Fig. 2 (center) as derived from a semi-empirical calculation. The perylene S0-S1 transition has strong HOMO-LUMO character [3] so that the LUMO wavefunction can be considered a good approximation to the excited state wavefunction. Fig. 2 refers to the free molecule, whereas in the actual system the molecule was attached to the surface of TiO_2. The proximity of empty isoenergetic electronic states in the TiO_2 conduction band can lead to a further extension of the excited state donor orbital right into the electronic states of the solid. Thus, a direct optical charge transfer contribution appears possible that is not included in the picture derived for the donor orbital of the isolated neutral molecule shown in Fig. 2. Nevertheless, the very different extensions of the chromophore´s donor orbital, i.e. onto the conjugated bridge but not onto the saturated bridge, are clearly borne out by the different chemical structure of the bridge units. For electron injection the latter functioned as insulator whereas the conjugated bridge as conducting molecular wire. The lower part in Fig. 2 shows the LUMOs of the oxidized dye molecules, which are the relevant electronic states in view of the recombination reaction. The striking difference compared to the excited states of the neutral molecules is the missing extension onto the bridge (marked with an arrow). Thus the conjugated and saturated bridge result in a very similar recombination rate (Fig. 1) that is dictated by the distance between the donor and acceptor. Expressed in the fancy language of molecular electronics, the sp2-hybridized bridge is wire-like in one direction of ET and insulator-like in the opposite, i.e it has some character of a molecular rectifier.

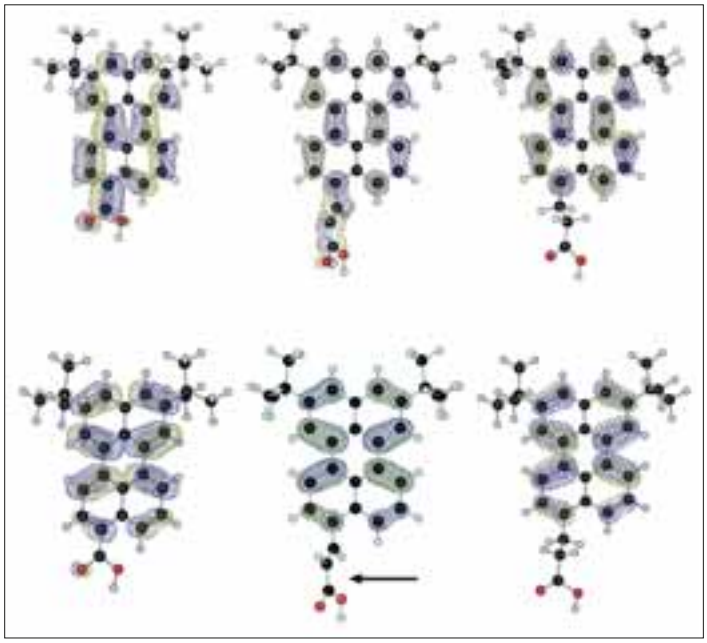

Fig. 2: Upper part: LUMOs of DTB-Perylene with three different bridge-anchor groups: -COOH (left),-CH=CH-COOH (center), and $-CH_2-CH_2-COOH$ (right). The energy of the LUMO for the neutral molecule is sufficiently close to that of the conjugated bridge and has pure π* character. The orbital representing the donor wavefunction extends onto the sp2-hybridized conjugated bridge unit (center) but not onto the saturated bridge unit (right). Lower part: β-LUMOs of the oxidized DTB-perylene compounds. In contrast to the LUMO of the neutral dye, the conjugated bridge is not involved in the MO. Wavefunctions calculated with ZINDO/S on a ZINDO/1 optimized geometry.

[1] Molecular Electronics, Edited by J. Jortner and M. A. Ratner, Blackwell Science, Oxford (1997)
[2] S. Ramakrishna, F. Willig, V. May, A. Knorr, J. Phys. Chem. B 107, 607 (2003); S. Ramakrishna, F. Willig, V. May, Phys. Rev. B 62, R16330 (2000)
[3] T. M. Halasinski, J. L. Weisman, R. Ruiterkamp, T. J. Lee, F. Salama, M. Head-Gordon, J. Phys Chem. A 107, 3660 (2003)

Corresponding author:
F. Willig
willig@hmi.de

Photocurrent injection into TiO_2 nano particles utilizing WS_2 quantum sheets

H. Tributsch, M. Thomalla
HMI, SE5

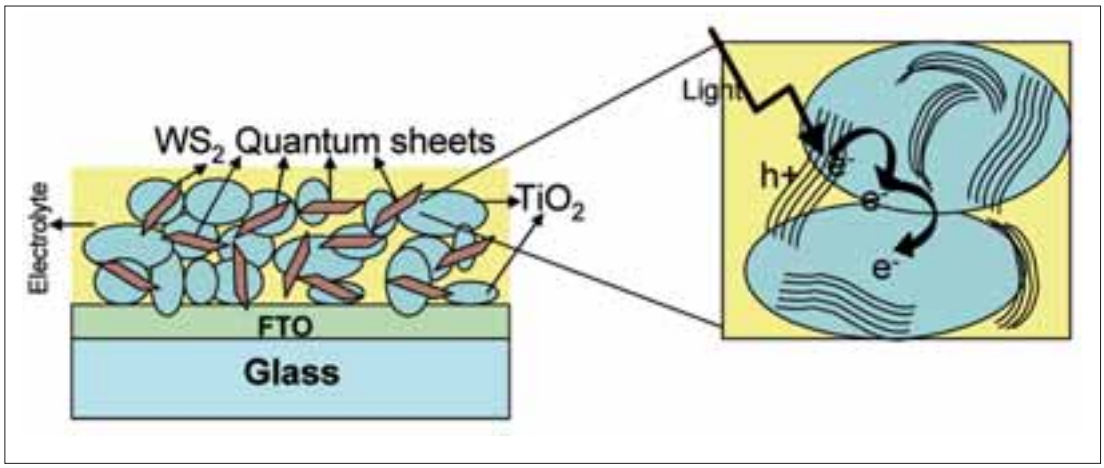

Fig. 1: Scheme of the TiO_2/WS_2 nano composite solar cell

Significant efforts have recently been undertaken to develop nano composit solar cells. They do not need well crystyllized materials and rely on chemical kineticall mechanismus for current rectification.

In particular, the solar cell developed by Grätzel and his group with its high solar energy conversion of up to 11% has increased the research efforts in this field [1]. A main problem with experimental nano composite solar cells up to now, both for dye solar cell and polymer/fullurene composite solar cell has been the long term stability. Unfortunately the original $cis\text{-}RuL_2(SCN)_2$ with L = 2,2'-bipyridyl-4,4'-dicarboxylatoacid (bpca) dye has not the desirable stability of 20 years [2, 3] and in addition the iodine/iodide redox system, the volatile solvent and its confinement pose problems.

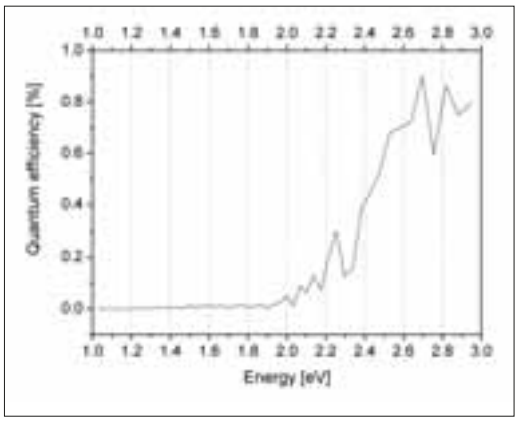

Fig. 2: Quantum efficiency of WS_2/TiO_2 cell

An interesting approach is to replace the organic dye with inorganic semiconductor quantum dots. Semiconductor quantum dots have several advantages. Firstly their band gap can be easily adjusted by changing the size of the particle to match the solar spectrum and the band gap of TiO_2. Secondly, they may be selected to posses a high absorbtion coefficient, which allows to produce very thin absorber and to reduce the amount of materials. And most important, it may be possible to apply a metallically conducting nano-contact as they are used in traditional solid state solar cells. In the presented work tungsten disulfide, which, due to its electronic structure, has been demonstrated to be a photochemically stable nano particle, has been investigated in a nano composite solar cell. The aim of this project is to sensitize porous, nanostructured TiO_2 (150 nm) with WX_2/MoX_2 (X = S, Se) quantum sheets (~5 nm) with the help of various chemical deposition methods. These substances have high absorbtion indexes (up to $3\times105\,cm^{-1}$) and single crystal WSe_2 photoelectrochemical solar cells gave efficiencies of 17% in iodine-iodide electrolyte [4]. The absorber has been characterized with help of EDX, TEM, REM, Raman spectroscopy and light absorbtion measurements. The photosensitization has been confirmed via electrochemical measurements. The surface of TiO_2 has been modified by a thin Al_2O_3 film, which significantly enhanced the photocurrent density, at solar light intensity, to $0.1-0.4\,mA/cm^2$. Moiré-patterns suggest that the S-W-S layers of WS_2 are not perfectly aligned in direction of c-axis, emphasizing the role of lateral electron transfer.

It is suggested, that WS_2 is deposited in the porous TiO_2 matrix as is shown in Fig. 1. The picture also visualises, how the electrolyte (I^-/I_3^-) regenerates the WS_2 sheets after photo induced electron injection into TiO_2 nano particle. When the WS_2 treated TiO_2 nano layer is exposed to an I^-/I^-_3 solution (propylene carbonate) and illuminated, photocurrents are indeed observed.

The spectrally resolved quantum efficiency of the WS_2 sample in LiI electrolyte is shown in Fig. 2. A clear contribution of visible light, confirming the photosensitization of TiO_2 by WS_2 nano layer, is observed. The onset of the photocurrent is at 1.8 eV, which corresponds to the direct band gap of WS_2 and also agrees with optical measurements. WS_2 induced photocurrents are observed in a solar cell arrangement but systematic research will be needed to better understand the mechanism and to achieve a significant improvement of efficiency.

[1] B. O'Reagan, M. Grätzel, Nature 353, 737 (1991)
[2] Helena Greijer Agrell, Jan Lindgren, Anders Hagfeldt Solar Energy, Volume 75, Issue 2, 169–180 (2003)
[3] M. Thomalla H. Tributsch IPS 15, Paris, Comptes rendus Chimie, in press
[4] O. Srivastava, G. Prasad, J. Phys. D: Appl. Phys. 21, 1028–1030 (1998)

Corresponding author:
H. Tributsch
tributsch@hmi.de

Self-organized nanostructures on silicon for photovoltaic applications

H. J. Lewerenz, S. Skorupska, M. Aggour, M. Kanis, M. Lublow, H. Jungblut
■ HMI, SE5

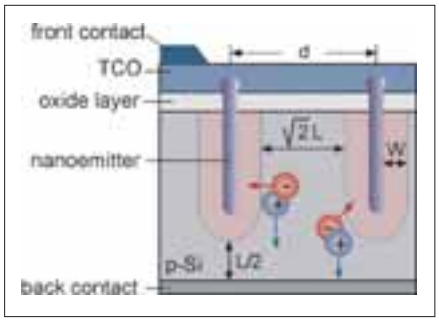

Fig. 1: Schematic of a Schottky-type nano-emitter solar cell; d, distance between pores; L, diffusion length; W, space charge layer width

Self organization allows large area preparation of surface features with sizes well below the limits of present lithographic methods. (Photo)electrochemical self organization occurs at low temperature under well defined conditions, such as applied potential, charge and current flow, illumination level, wavelength and solution composition that enable reproducible fabrication of micro- and nanotopographic patterns. Although regular topographies with micrometer dimensions could be prepared [1], analogous achievements in the nanometre domain have not yet been realized. They necessitate (i) empirical research, (ii) detailed knowledge of the silicon (photo)electrochemistry and (iii) analysis of results for possible applications. A schematic of an envisaged solar device is shown in Fig. 1: excess minority carrier collection occurs through nanometer-sized Schottky contacts, spaced in relation to the minority carrier diffusion length that are contacted to the front TCO [2]. Schottky nanoemitters can be fabricated by metal deposition into nanopores.

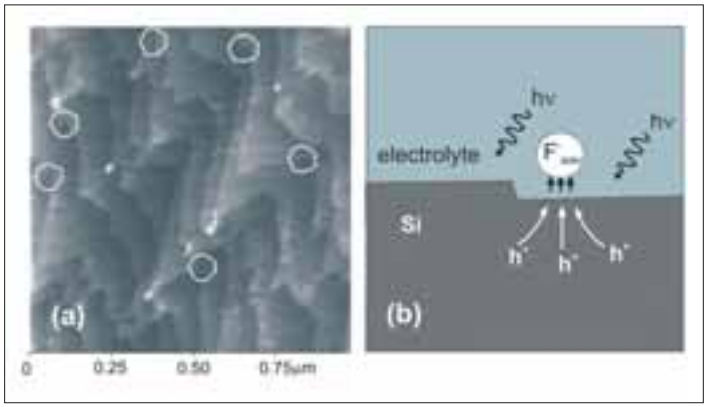

Fig. 2: Nanopore initiation at re-entrant sites on Si(111) obtained by CM AFM (a) and schematic of localized oxidation (b)

Spontaneous initiation and subsequent propagation of nanopores has been observed in series of fundamental studies of Si dissolution in acidic and alkaline electrolytes [3]: on (1×1) H-terminated Si(111), first nanopitting is seen at the re-entrant sites of the structure (Fig. 2a). Pore initiation is attributed to local electric fields between Si and counter ions, immobilized at specific sites above the surface, determined by DLVO and non-DLVO interactions [4]. The focussing effect of the electric field leads to minority carrier deflection to these sites, local oxidation of Si atoms and dissolution (Fig. 2b).

Corresponding deconvoluted SRPES (synchrotron radiation photoelectron spectroscopy) data (Fig. 3) reveal postulated dissolution reaction intermediates and a signal for the higher oxidized fully coordinated Si at the pit formation site ($\Delta E_b = 3.6\,eV$).

Pore propagation is facilitated for Si(001) where pore walls perpendicular to the surface are <110> oriented. Electrolytic (1×1) H-termination results in stable pore side walls and nanopores of rectangular shape. In a combined photoelectrochemical and chemical experiment, such nanopores have been prepared: first, Si(001) was made to oscillate at high anodic potentials in acidic electrolyte. The surface is then covered by $a \sim 10\,nm$ thick oxide that exhibits tiny cracks and pores (Fig. 4a). In KOH, the Si substrate is locally etched where the pores connect electrolytically. A subsequent HF dip removes the oxide layer leaving the imprint of the beginning nanopore propagation on the Si surface (Fig. 4b).

For efficient solar cell preparation, the pores should penetrate deeper into the absorber according to Fig. 1. Then, (photo)electro-deposition of a Schottky barrier metal into the pores produces the nanoemitter wires. The average pore distance can be controlled via the current phase at emersion. Such cell can be prepared self-organized at low temperature with three successive solution treatments. Generally, the nanopore distance allows usage of low diffusion length material. Recombination processes at the Si/metal and Si/SiO_2 interface, however, have to be controlled.

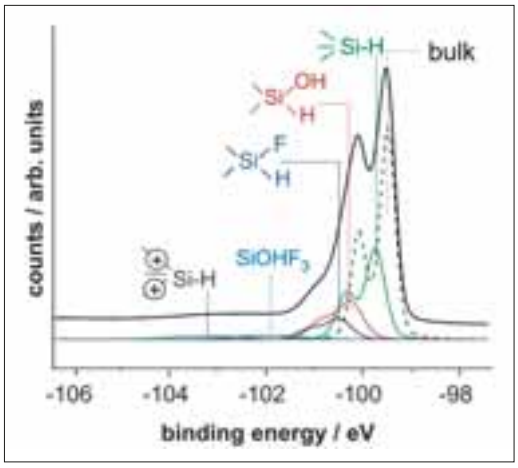

Fig. 3: SRPES of Si(111) after divalent photo-dissolution in ammonium fluoride electrolyte

This can be done by oxidation prior to metal deposition into the pores and by oxide annealing, respectively.

At cathodic potential, so-called step bunching is observed in alkaline solution. Up to 5 nm high terraces are formed on n-Si(111) [5]. SRPES shows that the surface is in accumulation, forming a two-dimensional electron gas (2 DEG) without front contact material. The Si 2p core level binding energy shift of 0.2 eV with increasing photon energy can be reproduced by calculation of the Thomas-Fermi screening potential for an electron concentration of $3\times10^{18}\,\mathrm{cm}^{-3}$ [5]. The AFM image in Fig. 5 shows the structure. Similar to the pore structures, the topography is of fundamental interest w.r.t. light coupling properties, which we investigate by Brewster angle analysis [6]. Also, relevant aspects of resistance quantization of 2 DEGs at low temperature can be investigated [7].

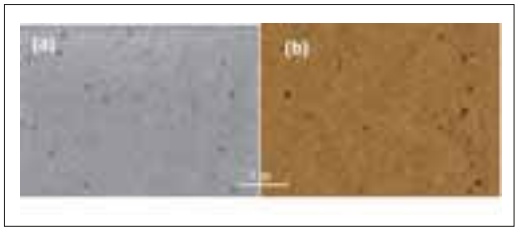

Fig. 4: Nanopore propagation experiments; (a) HRSEM image of pores in heterogenous oxide after current oscillations; (b) AFM image of pore growth into Si in alkaline medium by three-step soft solution technique

Regular oxide patterns with nanometre dimensions have been obtained in the region of negative resistance of the photocurrent-voltage characteristics of Si(111) in dilute acidic HF containing electrolyte. A typical image is shown in Fig. 6 after saturation oxidation on air. Regular, brick-type features are spread across the surface that can be comparibly easily removed by an AFM tip, allowing regular oxide and bare silicon patterning.

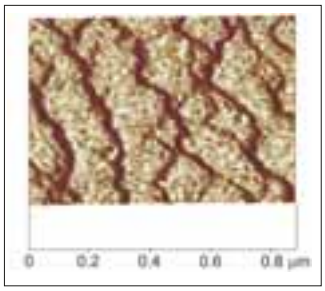

Fig. 5: CM-AFM image of a step-bunched Si(111) surface

Finally, it should be noted that the produced patterns are also important for immobilization of biological molecules, such as enzymes (proteins). Very little is known about protein-semiconductor junctions or interactions, and research in this area can lead to substantial advances in the field of proteomics.

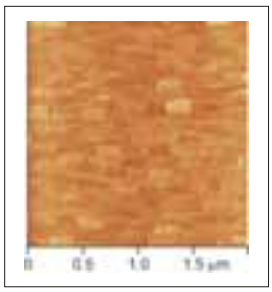

Fig. 6: AFM image of anodic oxide patterns after photoelectrochemical conditioning in 0.1M NH4F

[1] V. Lehmann, U. Gösele, Appl. Phys. Lett. 58 , 856 (1991)
[2] H. J. Lewerenz, Patent application DE, Az 103 47 401.3 (2003)
[3] H. J. Lewerenz et al., J. Electrochem. Soc. 150, E185 (2003); K. Skorupska et al., Electrochem. Commun. 7, 1077 (2005)
[4] B. V. Derjaguin, L. Landau, Acta Physicochimica (USSR) 14, 633 (1941); E. J. Verwey, J. Th. G. Overbeek, Theory of the Stability of Lyophobic Colloids, Amsterdam, Elsevier (1948)
[5] M. Krcmar et al., Phys. Rev. B 61, 13821 (2000)
[6] K. Skorupska et al., Appl. Phys. Lett 87, 262101 (2005)
[7] M. Lublow, H. J. Lewerenz, Transactions of the Institute of Metal Finishing 83, 238–247 (2005)
[8] K. von Klitzing et al., Phys. Rev. Lett. 45, 494 (1980)

Corresponding author:
H.-J. Lewerenz
lewerenz@hmi.de

Electronic structure of epitaxial ZnO thin films grown by MOMBE

S. Andres, C. Pettenkofer
HMI, SE6

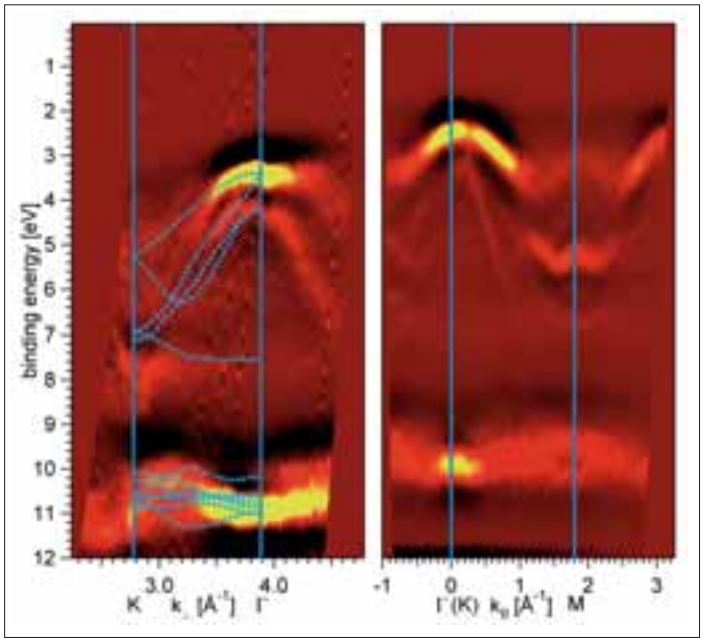

Fig. 1: ARUPS data of an annealed ZnO(11-20) film grown on r-plane sapphire. Dotted lines indicate a theoretical band calculation after Vogel et al.[1], which has been adapted to our measured data.

Optically transparent semiconductor compounds such as ZnO have gained considerable interest lately due to a variety of possible applications in the field of laser diodes, displays and solar cells. Molecular beam epitaxy is the growth method of choice for producing well-defined high quality monocrystalline layers. While the bulk electronic structure of ZnO was investigated in the past, a firm understanding of the surface and interface electronic properties is still an issue in ongoing research. In this report, we focus on the deposition of ZnO thin films on sapphire (Al_2O_3) as well as on SiC.

ZnO films were deposited in a UHV-MOMBE system from the organic precursor diethylzinc and water at growth pressures in the 10–5 mbar range at a deposition temperature of 450°C. As substrates, the r-plane of the Al_2O_3 single crystal and n-type 6H-SiC(0001) were chosen.

Samples were grown and characterized in situ by photoelectron spectroscopy (UPS, XPS) and low energy electron diffraction (LEED) without breaking the vacuum.

On the r-plane of Al_2O_3 ZnO grows epitaxially exhibiting the (11-20) surface. Especially the glide plane symmetry of the substrate is transferred to the growing film, as could be observed in the LEED patterns. Thus, an existence of different domains in these films can be ruled out. Concerning the chemical analysis, XPS data show no residuals of carbon in the film, which proves a clean reaction of the precursor substances. In the O1s spectra an admixture of about 5–10 % hydroxide is found which can be removed by annealing to 600°C. Valence band spectroscopy (UPS) reveals a change in the O2p band upon annealing such that the resulting spectra resemble those of a clean bulk crystal surface. Since this change is more predominant in the more surface sensitive HeII spectra we conclude that the as-grown films incorporate hydroxide at the topmost layers. Atomic force microscopy (AFM) scans of the surfaces obtained ex-situ show a film surface roughness of 2 nm which reduces to 1.5 nm after annealing. The carrier concentration n is found to be below 10^{-19} cm^{-3} with mobilities above 13 cm^2/Vs.

Fig. 1 displays angular resolved UPS data of an annealed ZnO(11-20) film. The spectra show a dispersion of the upper bands which are assigned to O2p derivatives. The dominant emission at a binding energy of about 11 eV corresponds to Zn3d bands showing weak but nevertheless considerable dispersion. A valence band splitting into 3 subbands is clearly visible for the $k_{\parallel}$ series (right hand side of Fig. 1). This can be explained by the hexagonal symmetry of the crystal field and the spin-orbit-interaction. For comparison, we have adapted a theoretical band calculation from the literature [1] to our data. The calculation exhibits an offset of about 2 eV for the Zn3d bands in comparison with our data. Consequently, in Fig. 1 we adapted these band calculations to the measured data.

In a second experiment we deposited ZnO on 6H-SiC (0001). The substrates were prepared by thermal annealing above 1000°C in hydrogen atmosphere and were transferred into the Integrated System under N_2. Here, a ZnO film was grown in consecutive steps in order to allow for an in-situ analysis of the changings in the interfacial properties (band bending, band offset) by XPS/UPS as well as the crystalline quality (LEED). Fig. 2 depicts the evolution of the substrate (Si2p emission), the film (Zn2p as well as O1s emission) and the valence bands. From the development of the corelevel lines in the course of deposition and the UPS spectra we obtained the band alignment at the interface ZnO(0001)/SiC(0001). Fig. 3 sketches the energetic offsets and displays the determined offset values.

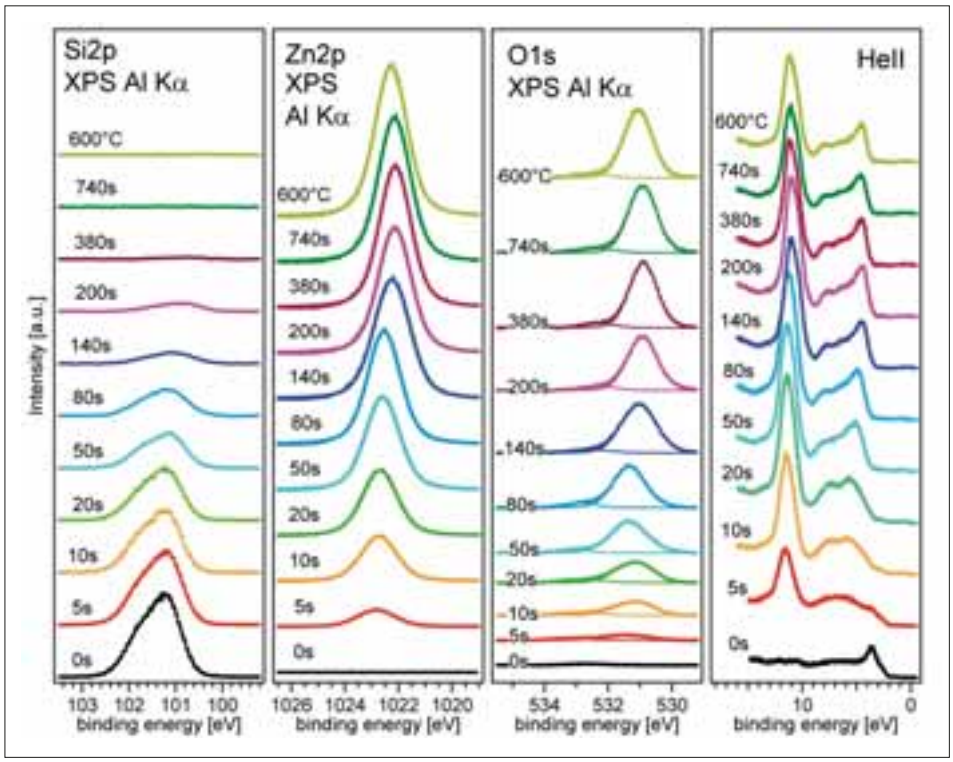

Fig. 2: Development of selected photoemission spectra with respect to stepwise deposition of ZnO on SiC(0001)

In conclusion, we have deposited well-defined monocrystalline ZnO films on sapphire and SiC using diethylzinc and water as precursors in our MOMBE system. The quality of the films is sufficient to obtain angular resolved photoemission data, which can provide a comparison with the electronic structure of bulk crystal surfaces. Using a stepwise deposition procedure in our integrated system we were able to determine the band alignment of the ZnO/SiC interface.

[1] D. Vogel, P. Krüger, and J. Pollmann, Phys. Rev. B 54, 5495 (1996)

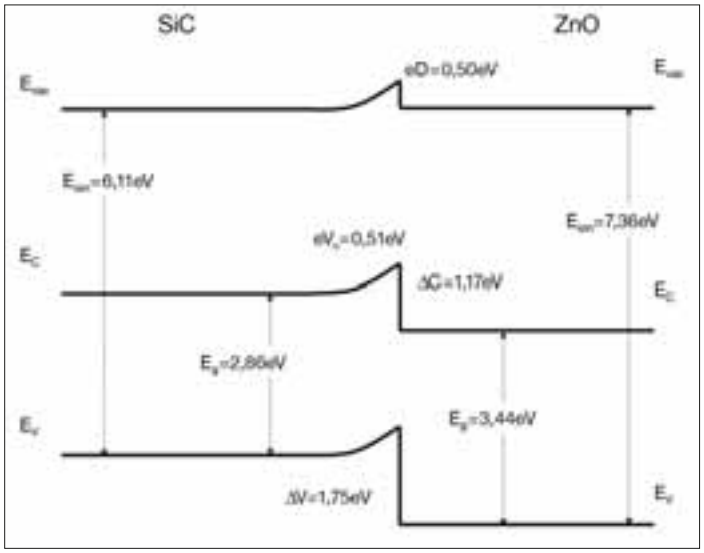

Fig. 3: Band alignment of the ZnO(0001)/SiC(0001) interface as determined from the photoemission spectra (cf. Fig. 2)

Corresponding author:
C. Pettenkofer
pettenkofer@hmi.de